ELSEVIER

Contents lists available at ScienceDirect

Journal of the European Ceramic Society

journal homepage: www.elsevier.com/locate/jeurceramsoc





Vat photopolymerization based Photoinhibition aided Ceramic additive manufacturing (PinCAM)

Yousra Bensouda, Yue Zhang, Xiayun Zhao

ZXY Intelligent Precision – Advanced Manufacturing (ZIP-AM) Laboratory, Department of Mechanical Engineering and Materials Science, University of Pittsburgh, Pttsburgh, PA 15261, USA

ARTICLE INFO

Keywords: Ceramic Additive manufacturing Photopolymer Photo inhibition Digital light processing

ABSTRACT

Vat photopolymerization (VPP) in ceramic additive manufacturing (CAM) faces challenges due to high viscosity from ceramic powder loading, necessitating interruptive recoating steps. Ceramic particles also attenuate and divert irradiated light, causing reduced cure depth and over-curing, leading to slow print, weak interlay adhesion, and dimensional errors. This study introduces photo inhibition-aided CAM (PinCAM) using dual-wavelength digital light processing to mitigate these issues. PinCAM employs two optical masks for initiation and inhibition at different wavelengths. While previous research focused on polymers, this work evaluates inhibition's effects in suspension-based VPP-CAM. Modeling and experiments examine inhibition and curing characteristics, print speed, dimensional accuracy, surface roughness, and microstructure. Preliminary results suggest that photoinhibition has the potential to enhance geometrical and surface properties as well as particle distribution homogeneity of green ceramic components without significantly compromising print speed. Understanding inhibition's impact will aid further research in PinCAM optimization for rapid and precise ceramic manufacturing.

1. Introduction

1.1. Ceramic materials and additive manufacturing

Ceramic materials are used extensively in a wide range of applications owing to their outstanding properties, such as high hardness and strength, good high-temperature performance, excellent thermal shock resistance, and high chemical stability. In aerospace, they are used to manufacture components like brakes, bearings, seals and even radiators for space vehicles; in the medical field, ceramics can be used for tissue engineering scaffolds, medical pumps as well as piezoelectric components [1]. However, due to the harsh conditions of ceramic production, the complexity of ceramic product design had been constricted by its limited fabrication methods. Due to mold restrictions, complex and customized shapes are almost impossible to produce without affecting the structural integrity of the final product [2,3]. While conventional manufacturing processes are unable to produce more detailed structures and typically require molds, ceramics also present unique challenges as a hard, brittle material [2]. Additive manufacturing (AM) technologies, also known as 3D printing, have potential applications in various industries such as aerospace, electronics, and bioengineering. Compared with conventional manufacturing, ceramic AM (CAM) can circumvent the limiting factors of ceramic material like high hardness and high melting point, as well as allow ceramic products of highly complex structures to be fabricated in a relatively short time without molds [4]. This opens a new door for the development of flexible yet strong ceramic parts.

Vat photopolymerization (VPP) is known to be one of the fastest, most accurate, and highest-resolution AM technologies with the possibility to print advanced products such as bio-renewable, light-weight, or electronic materials [5,6]. VPP involves the conversion of liquid photo responsive resin into sequential solid layers that are selectively cured by a light beam via photopolymerization [3]. During the photopolymerization process, the photo-initiators in the curing light act as catalysts. This triggers the irreversible formation of chains of polymers (cross-links) among monomers and oligomers present in the photopolymer [7–9]. Conversion of the liquid into solid parts happens in sequential layers. This method allows for the production of a variety of applications from soft hydrogels to strong flexible electronics. VPP-based AM offers new viable paths for the 3D printing industry, allowing the design of higher performing devices in numerous fields [10].

E-mail address: xiayun.zhao@pitt.edu (X. Zhao).

 $^{^{\}ast}$ Corresponding author.

VPP has been adapted to ceramic manufacturing by adding ceramic powders to the resin, creating various VPP based CAM (VPP-CAM) processes which have been proven capable of overcoming the challenges generally associated with the traditional production of ceramics with complex 3D shapes [11,12]. While VPP-CAM can overcome limiting factors of the material such as high hardness and low toughness, it does not come without its own challenges compared to the conventional VPP processes that handle homogeneous and transparent resins. In VPP based CAM (VPP-CAM), a slurry or semi-liquid mixture where ceramic feedstock powders are dispersed into liquid photoactive resin is printed by using a light beam to selectively cure the resin and form a matrix to bind the ceramic particles into a green ceramic part that will be subsequently sintered into a final part [13,14].

The VPP process is known to be a fast and accurate polymer AM method, but not so in the case of VPP-CAM. First, the use of ceramic powder can induce a high viscosity, which consequently requires recoating of the material. This technology therefore has limitations regarding the speed of the overall print process and the geometric accuracy of the final product. Second, the ceramic suspension in VPP-CAM is translucent and can largely attenuate and divert the light beam as it passes through due to complex interactions among light and ceramic particles including absorption, reflection, diffraction, and scattering [4]. The light attenuation will dramatically decrease the cure depth, and the light diversion (also referred to as general light scattering [15,16] in the remainder of this paper) will significantly increase the lateral over-curing in a VPP-CAM process [17]. Moreover, high solid loading is often desirable in VPP-CAM to effectively decrease the porosity of the sintered final part, accelerate de-binding, and reduce sintering shrinkage [2]. However, associated with high solid loading is high viscosity, a property that makes printing more difficult due to reduced flowability in the resin, often requiring a time-consuming recoating process between layers [12] due to an inability to re-level with the effects of air pressure and gravity alone [3], increasing amounts of solid loading cause an increase in light attenuation and scattering as it runs into the densely packed ceramic particles. With the use of higher solid loading, it can be expected that the lack of sufficient depth of curing would require printing a thinner layer each time to ensure sufficient inter-layer bonding strength but at an expense of severely delaying the total print time. Meanwhile, the lateral over-curing would become increasingly difficult to tackle as the solid loading increases.

Therefore, there is a great need for continuous, precise, accurate VPP-CAM processes to advance ceramic manufacturing and meet the demands for ceramic products and applications.

1.2. Current state of ceramic printing using photopolymerization

Digital light processing (DLP) is a mainstream VPP process with higher print speed and resolution than other VPP processes. Researchers have been adapting state-of-the-art DLP based VPP technologies for advancing ceramic 3D printing by using digital photo masks and photochemistry mechanism but just printing out of a vat of ceramicresin slurry [18]. Such DLP based CAM (DLP-CAM) processes are expected to inherit the advantages of polymer-based DLP [19,20]. However, it also carries the challenges due to the presence of ceramic particles incurred in general VPP-CAM as introduced in Section 1.1.

As DLP-CAM is far from maturity, research is ongoing to advance it from different perspectives and via different methods [21,22]. To decrease the effect of light attenuation and scattering in VPP-CAM, the most common approach is to adjust the resin formulation by using a non-reactive light absorber, which reduces the penetration depth and over-curing [11,12,23,24]. To address the issues of high viscosity and slow speed, a top-down continuous liquid interface production (CLIP) approach [10] is developed. In this approach, the oxygen-induced dead zone is above rather than below the printing part and the print head moves top down rather than bottom up. It has been employed to accelerate the printing of dense SiOC ceramic components by using a

natural continuous interface directly exposed to air (oxygen) rather than having a constrained closed interface as in the original version of CLIP [14]. But the oxygen inhibition in top-down DLP is uncontrolled [25], causing nonuniform layer thickness and inhomogeneous surfaces and requiring more exposure time [1]. To reduce the horizontal over-curing, in addition to optimizing the precursor formulation, another approach of research interest is to develop optimal greyscale mask projection that can refine the print without compromising the build, but this needs further investigation to understand its direct correlation [26,27]. Pattern density, exposure time and number of greyscale values used are all parameters that should be combined optimally to determine the best fit that will achieve best print quality, resolution and efficiency [28]. In fact, various shapes and geometries require the use of different greyscale masks, depending on the type of resins used as well as their photopolymerization properties. Moreover, while the greyscale mask projection can improve the print resolution, achieving high-quality surface finishes remains challenging. A more sophisticated method has been attempted to combine DLP and the two-photon polymerization (TPP) for CAM, yet it is costly and has a rather complicated implementation [29, 30]. Other methods of improving DLP-CAM include the use of adaptive layer thickness [31], as well as software-generated smart support systems [32-34]. However, these methods are facing drawbacks of limited materials or low production scalability with the printed part being only a few microns, opening the door for further study.

Overall, there is a critical lack of efficient and effective DLP-CAM methods to simultaneously increase print speed as well as reduce over-curing, especially lateral over-curing thus improves 3D geometrical accuracy.

1.3. Objective of this work

Recently, researchers have demonstrated that a photopatterned inhibition zone, which is thicker than oxygen inhibition zone in CLIP, can be induced by a separate light beam with a wavelength distinct from the photopolymerization light and used in DLP to enhance the print speed further, and even better, can achieve localized voxel thickness control [35]. Such a photoinhibition aided DLP process holds promise to be adapted to achieve fast and accurate DLP-CAM, thereby enhancing the design freedom. However, no literature reports are available to explicitly investigate the effects of photoinhibition in the specific scenario of ceramic slurry printing. To fill this gap, this work aims to initiate a systematic study on photoinhibition aided CAM for enhanced understanding and wider application of such a potential technology.

In this work, we present an initial, systematic study on a novel twowavelength irradiated, photopolymerization-based and photoinhibition aided DLP-CAM process, referred to as PinCAM. Unlike existing VPP-CAM methods (Section 1), PinCAM uses two optical masks with disparate wavelengths and adjustable intensities, thus allowing for more control over the curing process, thanks to the use of two wavelengths rather than a single one, to attain desired part properties and print speed. In current bottom-up DLP-VPP processes that are subjected to constrained liquid interface, the print speed and part quality tend to vary due to the adhesion or suction force between printed part and resin substrate. Whereas in PinCAM, the photo-inhibitor induced inhibition zone (or dead zone) can help reduce the separation force between the resin substrate and printed part, thereby improving the print speed and printed part's geometrical properties (e.g., surface roughness, shapes and dimensions, and resolutions). Adjusting the intensity ratio of the inhibition and initiation lights (e.g., UV and blue lights in this work) can change the inhibition zone thickness thus reducing the vertical separation force and interfacial shearing force. On one hand, thicker inhibition zone is desired to further ease the substrate-print separation thus accelerating the print and preserving the interfacial surface features. Moreover, increasing inhibition can help decrease over-curing for attaining better geometrical conformance. On the other hand, since the print speed of a DLP-VPP process depends on layer exposure time, more

inhibition necessitates greater exposure to ensure sufficient curing for strong interlayer bonding and to avoid defects (e.g., deformations, delamination, and cracks). As such, a dilemma exists while attempting to apply photoinhibition in DLP-CAM for simultaneously improving the print speed and geometrical fidelity. To unravel the paradox, we report a preliminary experimental study that is needed to understand the relationships among photoinhibition, photopolymerization, print speed, and geometrical properties with a focus on vertical and lateral dimensions accuracy. This work will shed some light on future work to establish PinCAM as an advanced ceramic manufacturing technology.

This paper is organized as follows: Section 2 details the methods, materials, and experiment setup, while Section 3 presents the experiment data analysis and results. Section 4 concludes the paper with discussion and recommendation for future work.

2. Methods and materials

2.1. Experimental setup of PinCAM

Our lab designed PinCAM system consists of two light sources (PRO4500PRO6500, Wintech Digital Systems Technology, Carlsbard, CA), which project two different light beams, one for polymerization (blue light: 460 nm) and photoinhibition (UV light: 365 nm). A two-wavelength mask is generated by combining two DMD projections of the two light beams via collimating optics and transmitted to a precursor vat. These two light sources are set up in junction with a movable build platform which has a linear stage (LTS 150, Thorlabs, NJ). An in-house LabVIEW software is developed to control both the photopolymerization and photoinhibition parameters - the irradiation intensity and pattern parameters accordingly as well as operate the build platform. Fig. 1 shows the PinCAM system setup.

In this work, grey scale masks of various light intensities for UV and blue light are created using a MATLAB code (see Figure A-1 in the

Appendix for masks). The projected shape into the precursor vat is a circle of a diameter of 6750 μm . Droplet feedstock via the use of a syringe guarantees a consistent, uniform resin layer, creating a mesh of interconnected polymers in the mixture [36]. The feedstock volume used for each print is 0.05 mL.

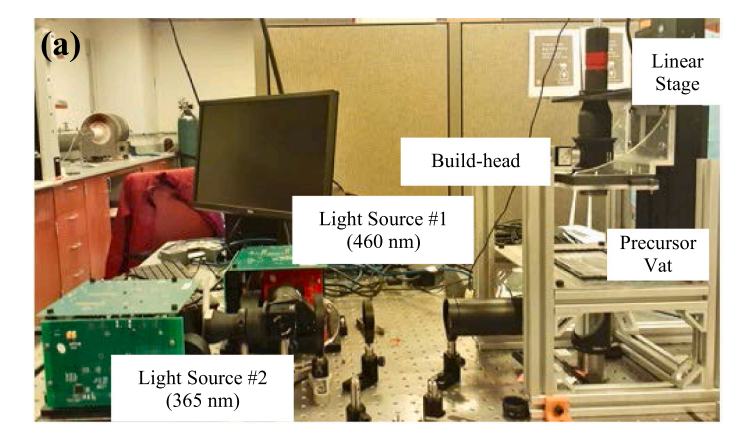
2.2. Feedstock material for PinCAM

Like regular VPP processes, PinCAM essentially relies on photopolymerization reactions to form the polymeric base for a green ceramic component. Meanwhile, photoinhibition is employed to confine the curing region for speeding the process and enhance the part properties. In this work, the photopolymerization is induced by photo-initiators - Camphorquinone (CQ) and Ethyl-4-(Dimethylamino) benzoate (EDAB), which act as catalysts to trigger the formation of polymer chains via the propagation of the reactive species that crosslink monomers - Triethylene glycol dimethacrylate (TEGDMA) and bisphenol A-glycidyl methacrylate (bis-GMA). On the other hand, the inhibition is prompted by the use of photo-inhibitors - free radical 2-(2-chlorophenyl)-4,5-diphenylimidazole (o-Cl-HABI) to control the curing [37].

The liquid resin is formulated as follows. Sigma-Aldrich is the provider for all the materials needed, which are used as received without further modifications. The chemical structure of the molecules is shown in Fig. 2.

- Monomers: 50 wt% TEGDMA, 50 wt% bis-GMA.
- Visible-light co-photo-initiators: 0.2 wt% CQ and 0.5 wt% EDAB.
- Free radical photo-inhibitor: 3 wt% o-Cl-HABI.

To prepare the ceramic slurry, 50 wt% (weight percent) Alumina powder consisting of Aluminum Oxide (Al_2O_3) with a mean particle size of 45 μ m and a purity of 99.9 % is mixed in 50 wt% of alcohol containing 0.05 wt% Stearic acid. The particle size distribution is



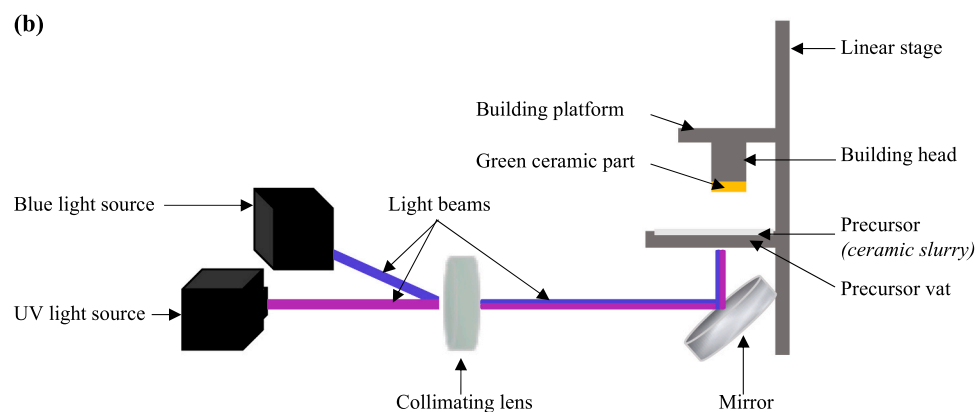


Fig. 1. Our in-house experimental system of PinCAM. (a) physical setup; and (b) schematic illustration.

Fig. 2. Chemical formulas of materials used this study. Monomers: (a) TEGDMA and (b) bis-GMA. Photo initiators: (c) CQ and (d) EDAB. Photo inhibitor: (e) o-Cl-HABI.

undisclosed by the manufacturer, while the particle shape is irregular. Please note that in this study's scope, we focus solely on evaluating the inhibition effect on the printing process and printed part properties. We operate under the assumption that the suspension is thoroughly mixed. with minimal batch-to-batch variations in particle size distribution. We ensure this consistency through meticulous preparation of the slurry and by utilizing the same batch of material for each experiment iteration, thereby excluding the influence of particle size variations in different PinCAM processing instances. Stearic acid is the dispersant, which stabilizes the mixture by homogeneously dispersing the Aluminum Oxide in the liquid medium containing alcohol. This prevents the settling and aggregation of the ceramic particles, since the Stearic acid creates a repulsive barrier between them, thus resulting in a uniformly distributed suspension which will not clump later. The ceramic suspension is stirred magnetically for 1 hour at a speed of 200 rpm, the later heated up to 80 degrees Celsius to remove any alcohol from the powder.

Finally, the PinCAM feedstock of ceramic slurry is obtained by mixing 50 wt% of the prepared liquid resin with 50 wt% of the ceramic suspension. The mixture is stirred magnetically at 30 degrees Celsius at a speed of 200 rpm for 1 hour.

Prior to the PinCAM experiments, the feedstock slurry is tested by an initial curing (see Fig. 3 below). Note that the purpose of this initial experiment is to verify the developed material system, not the PinCAM process. Therefore, no inhibition is used, and the curing condition is not necessarily optimized, accounting for the observed deformation. The part size increases with the increasing print time; however, the light pattern and intensity remain the same. This is mainly due to the overcuring issue introduced in Section 1. In the main experiment as presented in Section 3, PinCAM will be demonstrated to be able to mitigate the over-curing issue.

Photopolymerization typically occurs in stages. It starts when light decomposes photo-initiators into active radicals R* and effective radicals. This is known as the decomposition phase (Eq.(1)). The effective radicals then activate the monomer functional groups M, forming active monomers RM* in the initiation phase (Eq.(2)). Propagation is when the active monomers RM* react with one another forming several polymer cross-links (Eq. (3)). Finally, the radicals react with each other, either joining in one radical chain (Eq. (4)) or transferring from one chain to another (Eq. (5)), resulting in the termination of the polymerization [35, 38–40].

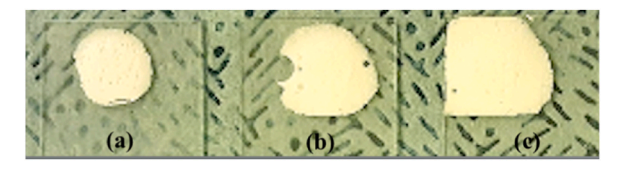


Fig. 3. Initial testing of the developed PinCAM feedstock material system. The curing time varies from left to right: 1 minute (a), 2 minutes (b) and 3 minutes (c) under a curing light with a circle pattern and an intensity of 4.73 mW/cm².

$$Initiator \xrightarrow{absorb\ photons} R*$$
 (1)

$$R* + M \longrightarrow RM*$$
 (2)

$$RM* + M_n \longrightarrow RM_{n+1}*$$
 (3)

$$RM_m * + RM_n * \longrightarrow RM_m RM_n$$
 (4)

$$RM_m * + RM_n * \longrightarrow RM_m + RM_n$$
 (5)

When using the feedstock of ceramic slurry, the photopolymerization process follows the same steps described [41]. Since the ceramic particles are dispersed in the liquid medium, they become trapped by the polymer networks once the photopolymerization starts. In fact, upon absorption of energy by photo-initiators after light exposure, the photopolymerization of monomers is triggered, causing the formation of a solid polymeric network. This polymer matrix plays the role of a binder, encapsulating the ceramic particles together to form the desired structure once the resin is fully cured. It is important to note that the green ceramic part formed will need to be sintered. This ensures particle consolidation, densifying the build. During this process, the ceramic particles undergo neck formation, where adjacent particles fuse together when they come into contact, thanks to the high temperatures used.

Fig. 4 shows the photopolymerization-based CAM process. After the light exposure, the monomers and ceramic particles are bonded by cross links, forming a solid when the liquid resin is fully cured.

2.3. Modeling the PinCAM process characteristics

Conventional VPP-CAM uses a single one-wavelength light source to activate photopolymerization. In contrast, our proposed PinCAM process uses a curing wavelength (460 nm in this work, denoted as I_{Blue}) to initiate photopolymerization, coupled with an inhibiting wavelength (365 nm in this work, denoted as I_{UV}) to simultaneously inhibit the curing reaction. Here, the inhibition zone height can be estimated by a literature model [35], as shown in Eq. (6).

Inhibition zone height:
$$H_{inh} = \frac{\log \frac{\beta I_{UV,0}}{I_{Blue,0}}}{\varepsilon_{UV} C_{UV} - \varepsilon_{Blue} C_{Blue}}$$
$$= \frac{\log \frac{\beta I_{UV,0}}{I_{Blue,0}}}{1/h_{UV} - 1/h_{Blue}}$$
(6)

 $I_{Blue,0}$ and $I_{UV,0}$ are the values of blue and UV light intensity incident at the bottom of resin vat, respectively. β is the inhibition coefficient - a lumped constant that incorporates the ratio of inhibitor to initiator absorption cross section, quantum yields, and reaction rate constants. ε_{UV} and ε_{Blue} are the UV and blue wavelength specific molar absorptivity of the absorbing species. C_{UV} and C_{Blue} are the molar concentrations of the UV-light-absorbing and blue-light-absorbing species, respectively. h_{UV} and h_{Blue} are the absorption heights of the UV and blue light, respectively. Generally, the absorption height at a certain wavelength is

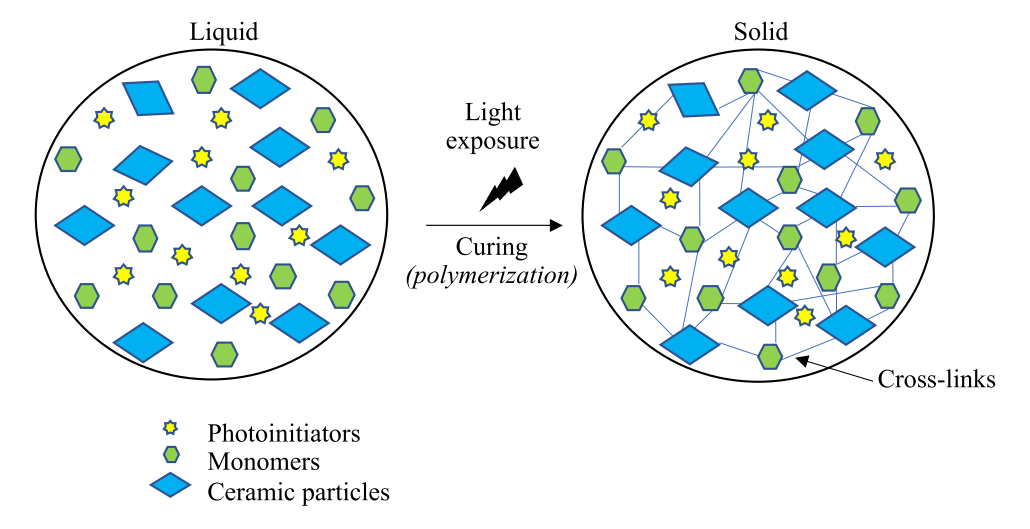


Fig. 4. Photopolymerization-based ceramic additive manufacturing process. Photo-initiators are excited by light radiation causing bonds between the different molecules to form. The radicals keep the polymerization going until the liquid polymer is fully cured.

defined as the inverse of the sum of the products of each absorbing species' molar absorptivity at that given wavelength and its molar concentration and is equal to the depth into a medium where each wavelength of light is 90 % attenuated. Specifically, in this work, we use one type of initiator and one type of inhibitor (Section 2.2), and the absorption heights can be calculated as below:

UV light absorption height:
$$h_{UV} = \frac{1}{\varepsilon_{UV}C_{UV}}$$
 (7)

Blue light absorption height:
$$h_{Blue} = \frac{1}{\varepsilon_{Rlue} C_{Rlue}}$$
 (8)

Cured height H_{cure} can also be related to the blue light absorption height as shown in Eq. (9), involving the ratio of the input energy dosage E_{input} and the critical energy E_c – minimum amount of energy needed for curing of the material (E_{input}/E_c) [42].

Cured height:
$$H_{cure} = h_{blue} \log \frac{E_{input}}{E_c}$$
, where $E_{input} = I_{Blue,0}t$ (9)

The maximum print speed S_{max} is estimated by a function as shown in Eq. (10). relating the absorption heights at each wavelength, h_{UV} and h_{Blue} , the intensity of those wavelengths, and the critical amount of energy E_c . These values and their relationship will supply a basis for optimizing print speed.

Maximum print speed:
$$S_{\text{max}} \propto \frac{I_{blue,0} h_{blue} - \beta I_{UV,0} h_{UV}}{E_c}$$
 (10)

It is worth noting that the values of inhibition constant β , initiator and inhibitor's molar concentration and absorptivity (thus absorption height), all depend on the precursor composition and light path. Experiment is needed to determine these parameters for each specific material formulation. More error and uncertainty are anticipated while characterizing these parameters for the more complex PinCAM process where the ceramic-resin slurry tend to be nonuniform in composition and deflect the light, in contrast to existing photoinhibition aided DLP-VPP [30,38] that handles only photo resin without solid inclusions.

2.4. Characterization of PinCAM-printed parts

In order to accurately characterize the dimensions and surface profile of printed samples, we use the Keyence VR-3200 Optical Profilometer – with a flexible optical microscopy and metrology platform. This system allows us to acquire and analyze with high precision the geometrical properties of the prints. Each sample's thickness and diameter are measured using this profilometer system with

representative image scans of some printed samples of green ceramic parts being shown in Appendix Figure A-2.

3. Results and discussion

To demonstrate the potential ability of PinCAM, it is essential to examine the inhibition and curing characteristics and their effects on print speed and dimensional accuracy. In this section, we present an initial experimental study to evaluate the correlation of the two-wavelength exposure intensities with the inhibition zone thickness, the working curve thus the critical energy and depth of penetration, as well as the print speed and as-printed ceramic part dimensions.

3.1. Inhibition zone characterization

As introduced in Section 2.3, studying the inhibition zone allow us to estimate the print size and speed thus optimize the two-wavelength exposures for accomplishing PinCAM. Knowing the inhibition zone height will also help determine a proper positioning of the build head in the vat to guarantee accurate control of layer thickness. To characterize inhibition zone, existing research on photo-inhibited DLP processes would cure samples within a simplified setup that comprises two glass slides with a spacer in between and then measure the cured sample thickness, from which the inhibition zone height is derived by subtracting the sample thickness from the spacer thickness [35]. However, the ex-situ setup might be different from the actual DLP print environment, since the spatial distributions of material composition and light energy within the curing chamber can vary due to the distinct precursor volume, species diffusion, and light transmission within a real DLP vat. Therefore, in this work, we will directly use the actual DLP build-head and vat separated by a constant spacer distance of 1000 µm, to form a chamber for charactering the inhibition zone more accurately.

Specifically, the ceramic slurry is exposed to (a pattern consisting of a circle of 936 pixels in diameter, corresponding to 6750 μ m on the vat) of co-incident UV and blue light for a constant period of time – 60 seconds. This pattern stays the same for all experiments in the subsequent sections, while the exposure time tested for is varied. Eight different I_{UV}/I_{Blue} ratios are chosen to study the variation of the sample thickness and consequently the inhibition zone as the UV and blue light intensity ratio changed: $I_{UV}/I_{Blue}=0$, 0.2, 0.4, 0.6, 0.8, 1, 1.2 and 1.4. The height of each cured sample is measured using the Keyence optical profilometer (see Appendix Figures A-3 and A-4). The corresponding inhibition zone height is determined by subtracting the cured thickness of each sample from the cured thickness values of the pure blue sample,

resulting in the inhibition ratio $I_{UV}/I_{Blue}=0$. While subtracting the cured thickness from the distance between the build-head and vat-substrate is another possible measurement method, we chose to use uninhibited samples that are generated using pure curing light (blue light in this study) as a reference to account for the overcuring issues and measurement difficulties caused by sample deflection.

Meanwhile, it is important to find out whether the individual curing light intensity I_{Blue} could affect the inhibition zone thickness given the same I_{UV}/I_{Blue} ratio. Although the models in Section 2.3 indicate that only the ratio determines the inhibition zone, we suspect that the species concentration might be affected by local curing and diffusion that is subjected to I_{Blue} . It is likely that species (e.g., initiators and monomers) concentrations would change significantly thus affect the inhibition zone as per Eq. (1). To understand the effect of curing light on inhibition zone, two sets of inhibition zone characterization experiment are conducted using two levels of curing light intensity (I_{Blue}), i.e., I_{Blue} = 2.45 mW/cm² and $I_{Blue} = 1.40$ mW/cm², with the same varying series of I_{UV}/I_{Blue} ratio. Each experiment set has three replications. Table A-1 in Appendix summarizes the experimental results at this stage. The plot of inhibition zone height in relation to the I_{UV}/I_{Blue} ratio and curing light intensity is shown in Fig. 5. We can see that the thickness of the inhibition zone increases logarithmically to the I_{UV}/I_{Blue} ratio.

From Fig. 5, we notice that using a lower light intensity of 1.40 mW/cm² allows to have a relatively larger inhibition height compared to the use of a light intensity of 2.45 mW/cm². We observe that samples do not cure for inhibition ratios larger than and equal to $I_{UV}/I_{Blue} = 0.8$, when a lower blue light intensity of 1.40 mW/cm² is used, even with an exposure time of 60 s.

For a higher blue light intensity of 2.45 mW/cm², the datapoint resulting from the use of a ratio of $I_{UV}/I_{Blue} = 0.2$, can be considered as an outlier due to potential measurement error. Moreover, the observed jump in the inhibition zone height for $I_{UV}/I_{Blue} > 1$, can be attributed to the intensity ratio being smaller than, but close to 1, which is approximately the threshold value of $\frac{1}{B}$ (derived from Eq. (6)). This threshold value causes a significant increase in the inhibition zone thickness. This possible threshold value is evident in the three similar inhibition zone thickness values observed when $I_{UV}/I_{Blue} = 0.4$, 0.6, and 0.8. Therefore, we adjust the curve-fitted parameters to disregard the average measurements for $I_{UV}/I_{Blue} = 0.2$ and observe a more suited trend. Indeed, when using a higher blue light intensity, curing is more dominant compared to inhibition, consequently, significant inhibition variations aren't observed for small ratios of $I_{UV}/I_{Blue}=0$ and $I_{UV}/I_{Blue}=0.2$. We notice an increase of the inhibition zone when choosing a ratio of I_{UV} / $I_{Blue} = 0.4$, with a continued exponential increase proportional to the ratio used, with the exception of $I_{UV}/I_{Blue} = 0.8$."

There are several possible reasons to explain these observations. Firstly, when the blue light intensity is low, the photo-initiators present in the feedstock resin may not absorb enough photons to reach their activation threshold. Consequently, the polymerization initiation is incomplete, resulting in lower curing thicknesses and higher inhibition heights. Moreover, during photopolymerization, the diffusion of photo-inhibitors is easier through less cured resin such as in the case of lower curing light, thus increasing the inhibition effect.

Moreover, by curve fitting with Eq. (6) in Section 2.3, we estimate the inhibition zone characteristic parameters including the coefficient β , and the absorption heights of UV and blue lights - h_{UV} and h_{Blue} , as shown

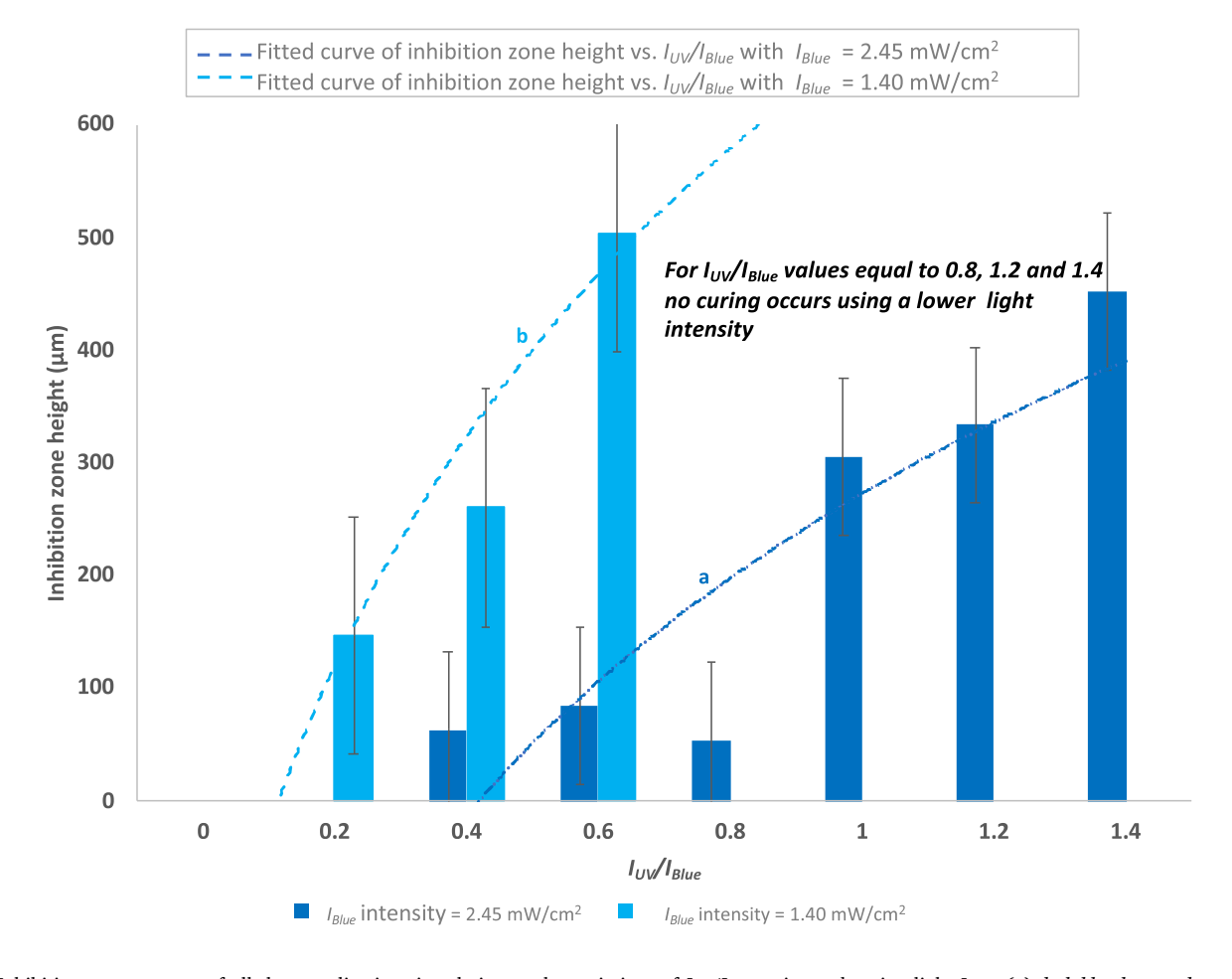


Fig. 5. Inhibition zone average of all three replications in relation to the variations of I_{UV}/I_{Blue} ratios and curing light I_{Blue} . (a) dark-blue bars and curve: $I_{Blue} = 2.45 \text{ mW/cm}^2$, (b) light-blue bars and curve: $I_{Blue} = 1.40 \text{ mW/cm}^2$.

in Appendix Table A-2. The absorption heights h_{IIV} and h_{Blue} are related to the energy light absorption of the liquid resin, while the inhibition coefficient β depends on its concentration. In this study, β is set to be 1 throughout the experiments with the resin composition remains the same as in literature [42]. Generally, the inhibition height is influenced by the absorption heights h_{UV} and h_{Blue} . A higher UV absorption height implies that the curing blue light energy is attenuated over a greater depth within the resin, resulting in a larger region where the curing reaction is inhibited. Conversely, a higher blue absorption height indicates a lower attenuation of the inhibiting UV light, as light penetrates deeper into the material. Indeed, blue light has lower energy and is absorbed more compared to UV light, the latter being more likely to cause electronic transitions and bond breaking. It is important to note that the variations of h_{UV} and h_{Blue} provide insights into the wavelength-dependent light absorption behaviors of the resin system. For a blue light intensity of 2.45 mW/cm², we observe an initial increase followed by a decrease and subsequent fluctuations in the blue light absorption height h_{Blue} . The UV light absorption height h_{UV} initially increases for an inhibition ratio of $I_{UV}/I_{Blue} = 0.8$, only to decrease again. A similar behavior occurs for a lower blue light intensity of 1.40 mW/cm². It appears that as the inhibition thickness increases (as seen in Fig. 6), the blue light absorption h_{Blue} decreases drastically, especially when using a lower blue light intensity; when the blue light intensity is lower, the decrease observed is slow.

Fig. 6 shows the absorption heights variations for both blue light intensities used. It also shows that at the I_{UV}/I_{Blue} ratio of 0.4 in the two cases of different blue light intensity, the UV absorption height value (h_{UV}) is negative while the blue light absorption (h_{Blue}) is especially high than the cases of other I_{UV}/I_{Blue} ratios. This unexpected result is conjectured to be because UV light might help cure the resin instead of inhibiting it under certain setting. In other words, the inhibitors could play the role of initiators under some light intensity or concentration ratio. The negative values observed are treated as outliers pending further study. More experiments are needed to confirm this finding.

Overall, the results of this experiment show that utilizing photoinhibition can reduce the curing thickness, and manipulating the curing light intensity and the ratio between curing and inhibition can help achieve the desired sample dimensions. Additional experiments and their corresponding results will be discussed in subsequent sections.

3.2. Working curve characteristics under the effect of inhibition

An important metric for studying photopolymerization is introduced by Jacobs as a standard design equation [43], and used extensively in literature to extract E_c and D_p from given experimental data [44]:

$$C_d = D_p \ln(\frac{E}{E}) \tag{11}$$

Where C_d is the curing thickness, D_p is the penetration depth, E is the energy of the light source and E_c is the critical energy.

To understand the curing behavior under the effect of inhibition, working curves of uninhibited and inhibited samples are measured during experimental PinCAM prints under different inhibition and curing intensity ratios – I_{UV}/I_{Blue} . Samples are printed for each given I_{UV}/I_{Blue} I_{Blue} ratio with the curing time ranging from 20 s to 60 s. Note that an increase in the exposure time is accompanied by an increase in the exposure energy dosage. Three replications are conducted for each experiment setting (i.e., under each set of I_{UV}/I_{Blue} and exposure time). As in those typical VPP processes, depth of penetration D_n and critical energy E_c are estimated from the experimental working curve fitting using Eq. (11) and shown in Appendix Table A-3. Appendix Figure A-5 shows an example of how the working curve data is retrieved and interpreted. By deriving these values, we can make predictions about the exposure energy and time required to achieve the desired thickness. More importantly, we can examine the trends of E_c and D_p under different ratios of I_{UV}/I_{Blue} .

Overall, the plots in Fig. 7 summarize the results. As the energy dosage increases, we can see an increase in the curing thickness for each. The increase is significant, and all ratios exhibit a similar trend for the two different I_{Blue} light intensities used. Both plots confirm the hypothesis as tested in Section 3.1 that while the I_{UV}/I_{Blue} ratio directly determines the inhibition zone, the curing light intensity I_{Blue} also affects its behavior, owing it to the changing concentrations of the interactive species which respond differently to the varying I_{Blue} intensities. For a curing intensity of $I_{Blue} = 2.45 \, \mathrm{mW/cm^2}$, samples cured without inhibition have higher heights than those with an inhibition ratio of I_{UV}/I_{Blue}

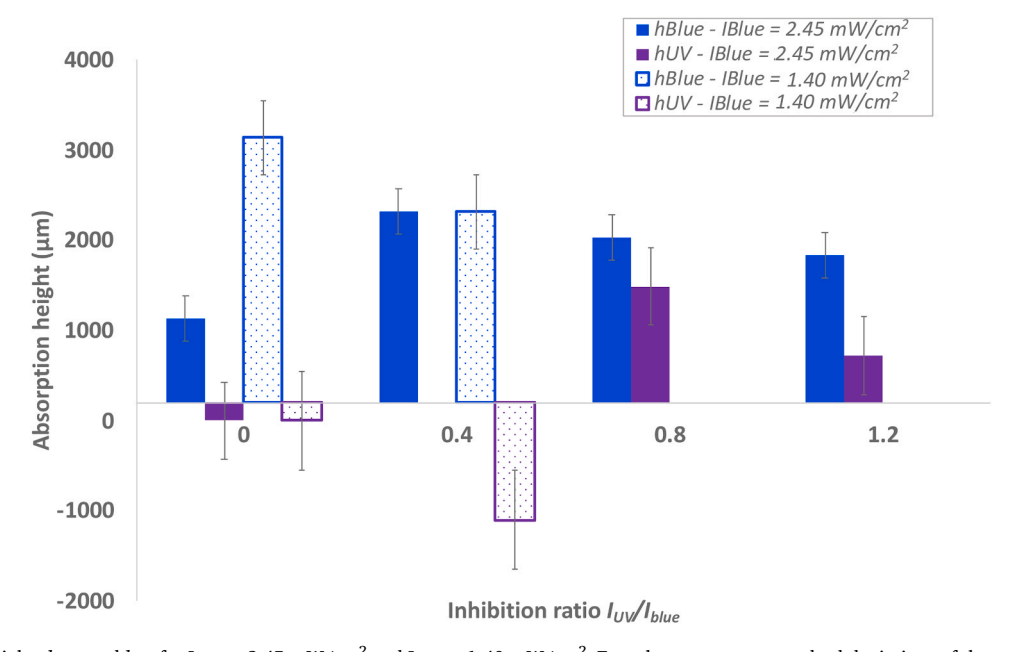


Fig. 6. Absorption heights h_{Blue} and h_{UV} for $I_{Blue} = 2.45$ mW/cm² and $I_{Blue} = 1.40$ mW/cm². Error bars represent standard deviations of three replications. For $I_{Blue} = 2.45$ mW/cm², the absorption height h_{UV} value observed is negative for an inhibition ratio of $I_{UV}/I_{Blue} = 0.4$, and therefore considered as an outlier not shown in the figure. Using a lower blue light intensity of $I_{Blue} = 1.40$ mW/cm², no curing occurs for $I_{UV}/I_{Blue} = 0.8$ and $I_{UV}/I_{Blue} = 1.2$, thus no corresponding plots for h_{Blue} and h_{UV} are shown.

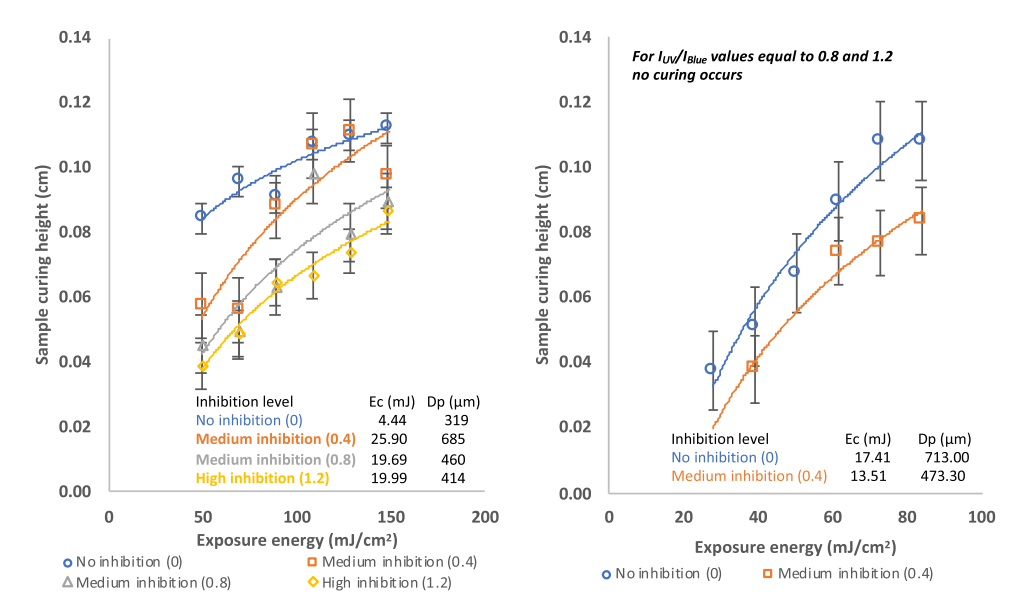


Fig. 7. Working curves under different inhibition and curing light exposures. Blue light intensity $I_{Blue} = 2.45 \text{ mW/cm}^2$ (left) and $I_{Blue} = 1.40 \text{ mW/cm}^2$ (right). (Note: The error bars represent standard deviation of three replications. E_c and D_p values are estimated by averaging the replications (see Table A-3).

= 0.4, followed by samples cured with a ratio of $I_{UV}/I_{Blue} = 0.8$, then lastly those with a ratio of $I_{UV}/I_{Blue} = 1.2$. Using $I_{Blue} = 1.40 \text{ mW/cm}^2 \text{ we}$ notice a similar trend, but lower sample curing heights compared to similar inhibition conditions with a higher blue light intensity (i.e., $I_{Blue} = 2.45 \text{ mW/cm}^2$ in this work).

From the experimental data, using an intensity of $I_{Blue}=2.45~{\rm mW/cm^2}$, we notice a significant increase in the critical energy values when introducing inhibition, followed by a slight decrease in the values which stabilizes. The penetration depth on the other hand increases when introducing inhibition – from 319 μ m to 685 μ m –, then starts to drop to 460 μ m after an inhibition ratio of $I_{UV}/I_{Blue}=0.8$, followed by 414 μ m for $I_{UV}/I_{Blue}=1.2$.

Further, we investigate the E_c and D_p under the same I_{UV}/I_{Blue} ratio but different curing light intensity (I_{Blue}). For a blue light intensity of 1.40 mW/cm², the critical energy starts to decrease once inhibition is introduced – decreases from 17.45 mJ to 13.51 mJ. The penetration depth decreases too, from 713 μ m to 474 μ m. However, nothing can be said about neither the critical energy nor the penetration depth for the inhibition ratios of 0.8 and 1.2 since no resin cures.

Based on the fact that an increase in inhibition results in a decrease in the amount of light reaching the sample, we deduce that a higher amount of energy is needed to supplement the inhibited radicals to achieve the desired polymerization. As such, the critical energy value E_c would increase with inhibition as shown in Fig. 7 (details in Table A-3). With lower critical energy, liquid resin gets cured more easily. Cured parts tend to absorb and scatter the curing light thus impeding the penetration of light through the material. As a result, the depth of penetration depth D_p is usually smaller in the cases that uses lower or even no inhibition and thus require less critical exposure energy. However, from Fig. 7 we also see that D_p tends to decrease as the inhibition ratio goes beyond 0.4. This could indicate that excess inhibition might cure the resin instead (corroborating our discussion about the observed negative h_{UV} in Section 3.1), thereby reducing the light penetration. While some of these observations are intuitive given the role of inhibition in PinCAM, it is worth noting that our experiment reveals the increase of E_c engendered as the I_{UV}/I_{Blue} ratio increases, while D_p values fluctuate between an increase and a decrease, suggesting a complex and delicate interplay of inhibition and initiation in PinCAM. Further investigations are needed and will include more detailed analyses to elucidate the underlying mechanisms and trends driving the observed differences.

3.3. Effects of inhibition and curing on PinCAM process and product

This subsection aims to understand the correlation of the inhibition and curing characteristic metrics with the PinCAM processing speed and its as-printed green parts geometrical properties including dimensional accuracy and surface roughness.

3.3.1. Geometric accuracy with a focus on tackling three-dimensional overcuring

To address the outstanding issue of over-curing in VPP-PAM (discussed in Section 1), we focus on evaluating the effectiveness of PinCAM in reducing over-curing in the lateral dimension by two metrics as follows. First, we focus on comparing the cured diameter against the diameter of the circle pattern projected on the platform (i.e., 6750 μm) to evaluate whether PinCAM can yield a lateral dimensional accuracy that is often overlooked in current research (see Section 1.2). Second, we aim to achieve the desired lateral diameter while minimizing the cured height and reducing exposure time. It's important to note that these experiments don't have a specific target height in mind; instead, the goal is to enhance vertical resolution and mitigate the inherent staircase effect associated with VPP.

Both the cured samples' diameter and height values are plotted as a function of exposure time for varying I_{UV}/I_{Blue} ratios and two levels of blue light intensities (Figs. 8 and 9). We observe a decrease in the values of sample diameter as inhibition increases. Although the diameter values are slightly lower than 6750 µm, they are still close to that value (Table A-4). For instance, using a blue light intensity of 2.45 mW/cm², samples have diameters of 6822 μ m ($I_{UV}/I_{Blue} = 0$, relative error = (6822-6750)/6750 = 0.01), 6558 µm ($I_{UV}/I_{Blue} = 0.4$, relative error = 0.02), 6287 μ m ($I_{UV}/I_{Blue} = 0.8$, relative error = 0.06) and 6240 μ m ($I_{UV}/I_{$ $I_{Blue} = 1.2$, relative error = 0.07) respectively, associated with an exposure time of 60 s. This clearly demonstrates that inhibition effectively reduces lateral over-curing but needs an optimal inhibition ratio as the case of $I_{UV}/I_{Blue} = 0.4$ seems to achieve the smallest relative error among all the tested ratios in this study. A higher blue light intensity allows us to achieve values that are closer to the target. Meanwhile, it is worth mentioning that even a lower blue light intensity of 1.40 mW/cm² reduces lateral over-curing. Indeed, a higher blue light intensity can ensure better results, as it provides more energy to initiate and complete the curing process. However, it must be carefully controlled to prevent overcuring, a concern that is typically more manageable when using lower light intensities.

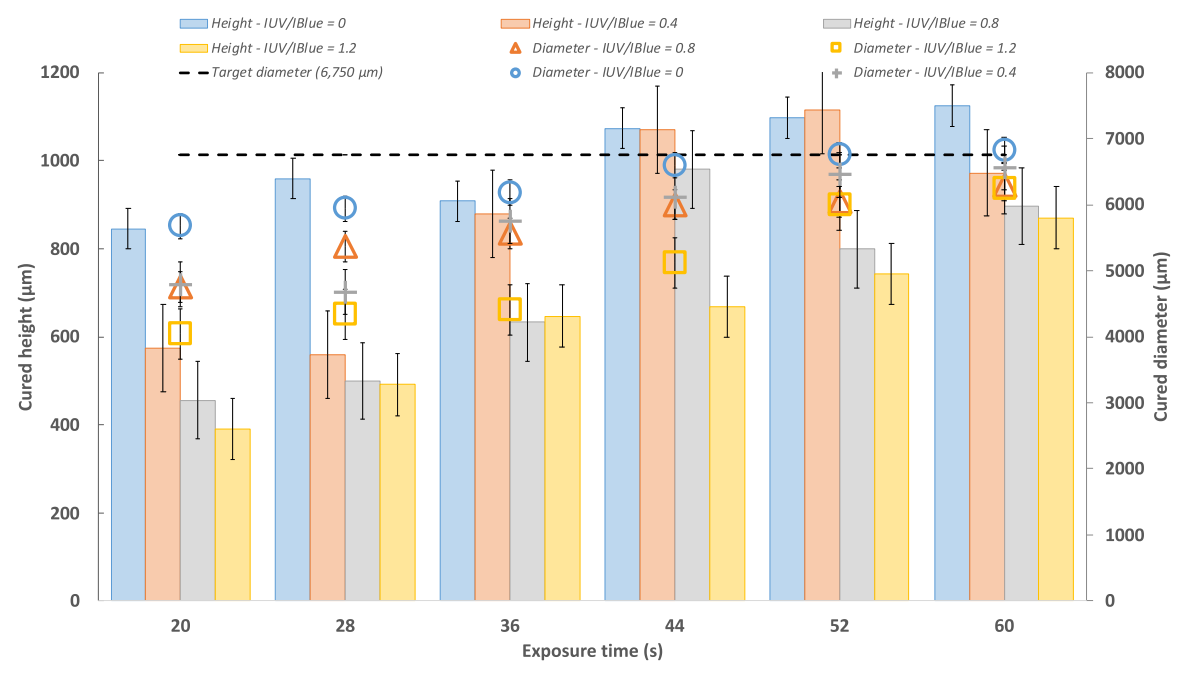


Fig. 8. Cured diameter and height varying with exposure time for a blue light intensity $I_{Blue} = 2.45 \text{ mW/cm}^2$ and all inhibition ratios (I_{UV}/I_{Blue}) tested.

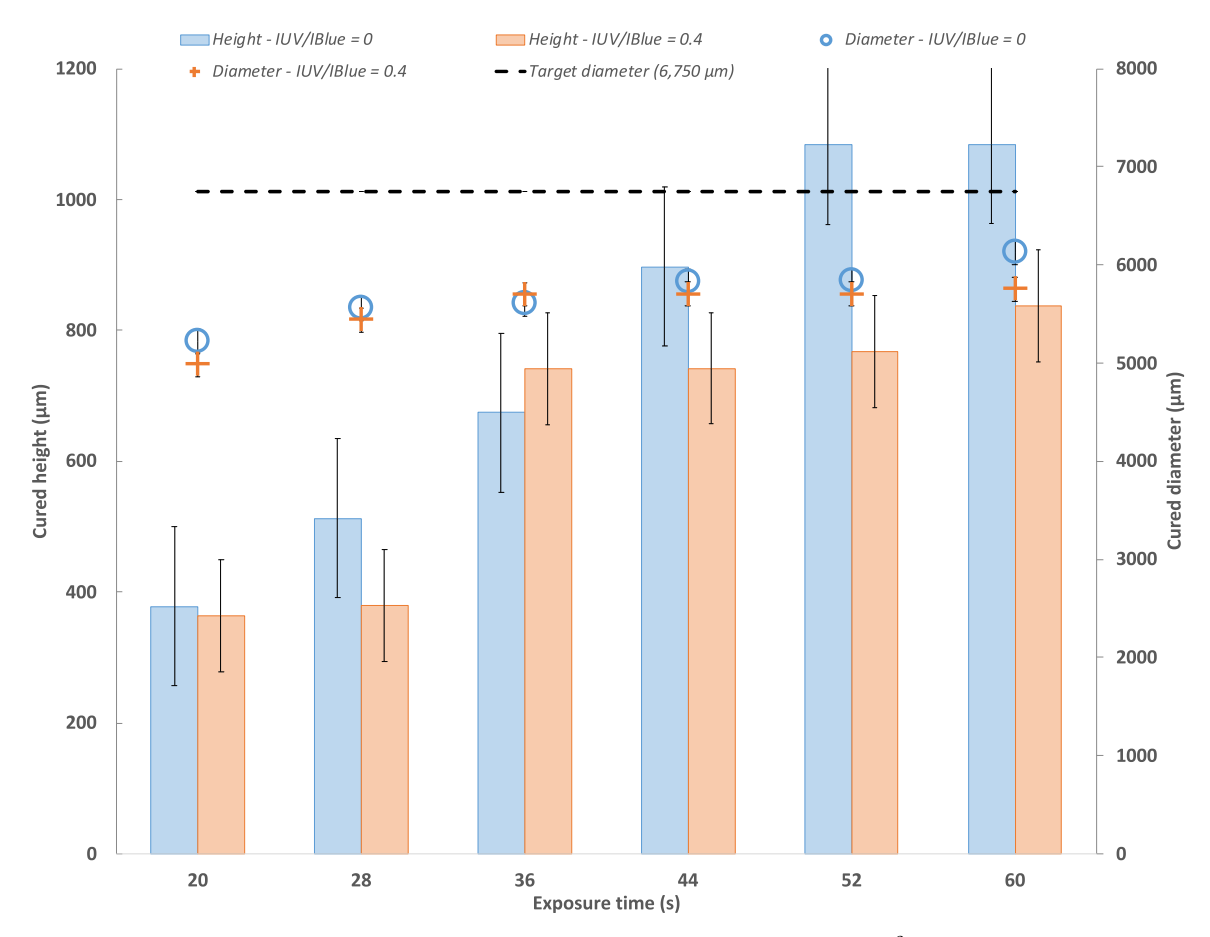


Fig. 9. Cured height and diameter varying with exposure time for a blue light intensity $I_{Blue} = 1.40 \text{ mW/cm}^2$ and all inhibition ratios I_{UV}/I_{Blue} tested.

Simultaneously analyzing the cutting height and diameter data allows us to see that while a custom diameter can be achieved by increasing exposure time, vertical over-curing heightens. Indeed, for a blue light intensity $I_{Blue} = 2.45 \ mW/cm^2$, using no inhibition level for an

exposure time of 44 s, the target diameter is best attained. However, the cured height exceeds $1000~\mu m$, which implies a too-low vertical resolution and a too-large layer thickness, leading to potential vertical dimensional error and staircase error in the final printed parts.

Introducing an inhibition (such as $I_{UV}/I_{Blue}=0.8$) would allow for a slightly larger diameter but smaller cured height. The same trend is observed in the case of using a blue light intensity of $I_{Blue}=1.40~mW/cm^2$, where an exposure time of 60 s is promising to reach the target diameter and an addition of inhibition can help bring down the vertical height. Although non-optimal results are accomplished yet in this work, these initial observations with encouraging trends indicate that optimizing the curing light intensity and inhibition ratio will likely be able to help VPP processing of ceramic parts with improved accuracy and resolution in all three dimensions. Future research on process optimization is recommended for establishing the promising PinCAM process.

Our results demonstrate a decrease in curing heights, because of an increase in the level of inhibition. By utilizing PinCPAM, we can effectively achieve the target height in a shorter exposure time, as inhibition reduces vertical over-curing.

Overall, when using pure blue light, the curing height reaches a maximum value – 1125 µm for $I_{Blue}=2.45~{\rm mW/cm}^2$ and 1084 µm for $I_{Blue}=1.40~{\rm mW/cm}^2$ – yet the sample is at a high risk of over-curing since there's no inhibition to contain the process (target values to mimic is 1000 µm). Using photoinhibition thus allows to have better control over the desired sample thickness. For an I_{UV}/I_{Blue} ratio of 0.4, the achieved thickness was 1070 µm and 972 µm for exposure times of 44 s and 60 s respectively, using a light intensity of $I_{Blue}=2.45~{\rm mW/cm}^2$. Using a blue light intensity of $I_{Blue}=1.40~{\rm mW/cm}^2$ on the other hand, allows to get a sample height of 837 µm, for an exposure time of 60 s, with the same inhibition ratio.

3.3.2. Surface roughness

Surface roughness directly affects the friction and overall build performance. In conventional VPP-CAM, either the recoating process or the suction force between the constrained surfaces of build head and substrate could highly influence the surface roughness. Herein, we aim to understand how photoinhibition in PinCAM can allow to achieve the desired surface quality of the build. To reiterate, the presence of the photoinhibition zone is expected to reduce surface imperfections, bumps and irregularities that could be caused while moving the print stage to separate the cured part from substrate.

Generally, the surface roughness is quantified by the arithmetic average roughness (S_a) , which provides information about the overall roughness of the surface. The value of S_a can be evaluated by the governing equation:

$$S_a = \frac{1}{l} \int |z(x)| \quad dx \tag{12}$$

where: l is the diameter of the sample to be analyzed, and $\int |z(x)| \, dx$ denotes the integral of the absolute value of the sample height z(x) evaluated over the sampling diameter. Fig. 10 below is a 3D image scan of the surface roughness of some cured samples. Since the arithmetic average roughness S_a is a good indicator of the variations, we rely on this parameter to determine how the surface roughness of the samples analyzed above changes with respect to varying exposure time for different inhibition levels, disclosing the potential role of inhibition zone in improving surface finish due to reduced interfacial force. Appendix

Figure A-6 illustrates the 3D surface roughness of a few samples obtained via the Keyence profilometer scans, where surface irregularities are evidently seen.

When using a blue light intensity of $I_{Blue} = 2.45 \text{ mW/cm}^2$, for a sequence of exposure times (20 s, 28 s, 36 s, 44 s, 52 s, and 60 s) as shown in Fig. 10 and Fig. 11, the medium inhibition ration of $I_{UV}/I_{Blue} =$ 0.8 gives the best surface finish overall. Low levels of inhibition may fail to generate a sufficiently thick inhibition zone, leading to significant suction forces between the slurry and the printed part, which can roughen the surface. Conversely, high levels of inhibition may markedly reduce curing, resulting in inadequate binding strength and more pronounced surface roughness. Therefore, it's not surprising that we observe the existence of a certain sweet spot where optimal medium inhibition yields the smallest surface roughness. Besides, Fig. 11 shows that samples cured for 36 s exhibit larger surface roughness than the non-inhibited sample cured for the same amount of time and the roughness increases with the inhibition ratio. This is the only case that shows such an abnormal trend compared to the other cases of different exposure times. When cured for 36 s only, the samples start to shrink as the inhibition level increases. This results in an increased surface roughness, as shrinkage causes internal stress within the material, leading to the formation of defects as the material tries to maintain its shape. Another possible explanation to this abnormality would be the light intensity variability and stability over time, which can result in uneven curing. However, further experimentation is needed in future research to uncover the exact underlying cause. With a light intensity of $I_{Blue} = 1.40 \text{ mW/cm}^2$, the results on surface roughness are not as conclusive as in the case of $I_{Blue} = 2.45 \text{ mW/cm}^2$, probably due to the relatively less-cured parts being more fragile to other environmental factors such as stage movement and resin flow (see Table A-5). In this case, although the surface roughness behavior fluctuates as the exposure time changes, most of the time the inhibited samples display lower roughness than the non-inhibited samples. As such, we can conclude the inhibition effects on surface finish are more tangible with higher light intensities (see Fig. 11).

All these observations imply that while inhibition is demonstrated to be capable of improving in-process layer surface smoothness (mainly due to increased dead zone thickness thus reduced suction force), there is a great need for finding an optimal combination of curing light intensity and inhibition ratio to achieve a good surface roughness in PinCAM.

3.3.3. Print speed

In order to understand how inhibition would affect the ceramic printing process, we evaluate the vertical print speed with respect to exposure time for the two light intensities I_{Blue} investigated in this study for varying inhibition ratios I_{UV}/I_{Blue} . (see Fig. 12).

It is intuitively understandable that in general the print speed is higher with lower inhibition as shown in the case of high curing light intensity ($I_{Blue} = 2.45 \, \mathrm{mW/cm^2}$) in Fig. 12. Meanwhile, it is interesting to find that at this curing light intensity ($I_{Blue} = 2.45 \, \mathrm{mW/cm^2}$), the non-inhibited speed (blue curve) will decrease as exposure time increases and tends to be flatter at longer exposure time (> 36 s in this case). This

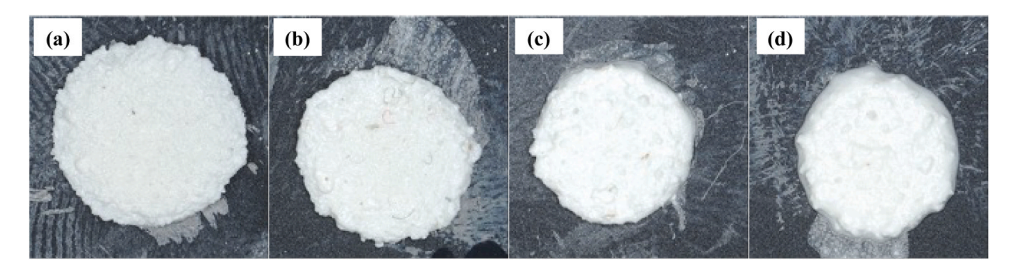


Fig. 10. Keyence VR-3200 images of samples cured under different inhibition conditions for an exposure time of 60 s: (a) $I_{UV}/I_{Blue} = 0$, (b) $I_{UV}/I_{Blue} = 0.4$, (c) $I_{UV}/I_{Blue} = 0.8$, (d) $I_{UV}/I_{Blue} = 1.2$. This demonstrates that inhibition allows to get smoother surfaces.

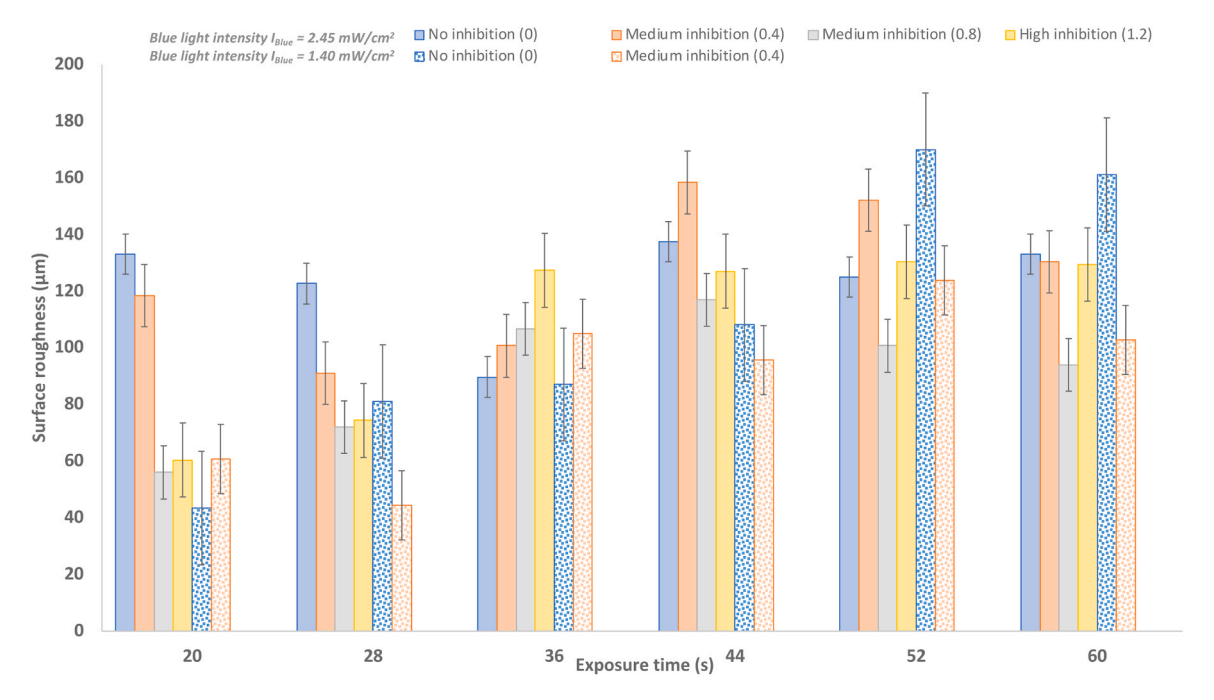


Fig. 11. Inhibition effects on surface roughness.

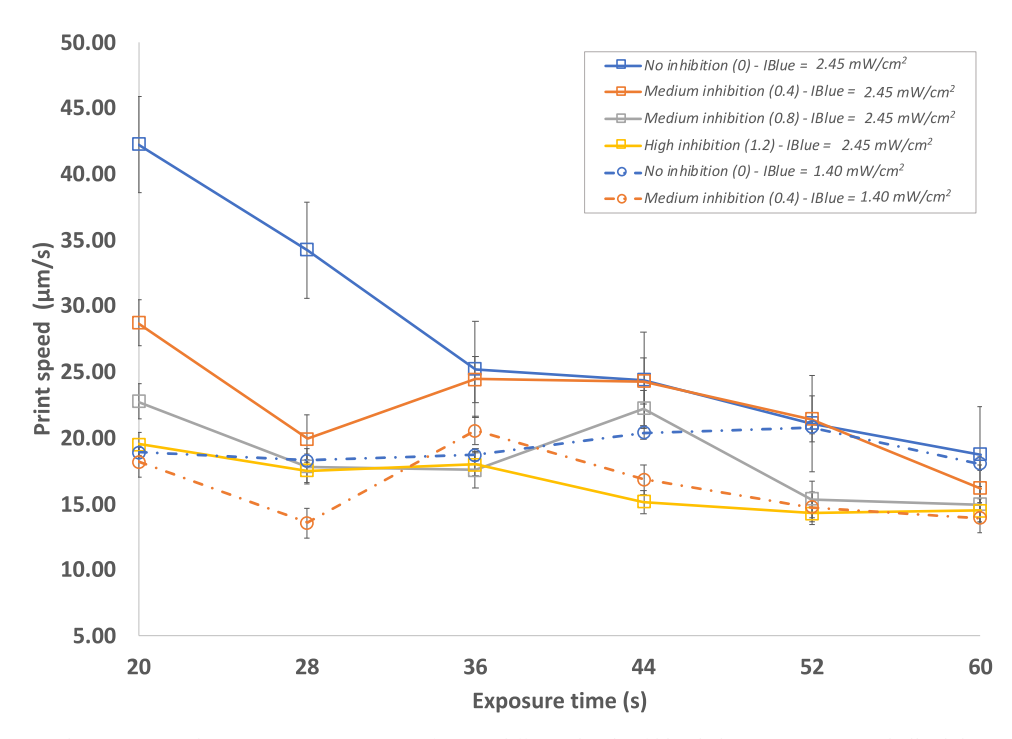


Fig. 12. Vertical print speed variations with respect to exposure time for two different levels of blue light intensity I_{Blue} and all inhibition ratios I_{UV}/I_{Blue} tested.

is probably due to the saturation of curing species such as free radicals. It also shows that the inhibited process speed could be close to the non-inhibited speed at certain exposure time with certain level of inhibition. For example, using a light intensity $I_{Blue} = 2.45 \, \mathrm{mW/cm^2}$ under a medium inhibition level of $I_{UV}/I_{Blue} = 0.4$ allows for printing the sample with similar speed to the pure blue light curing at exposure times of \geq 36 s. It is worth noting that this combination of inhibition ratio 0.4 and exposure time of 36 s gives rise to a potentially near-optimal setting for tackling over-curing (see Section 3.3.1).

In the case of a light intensity of $I_{Blue} = 1.40 \text{ mW/cm}^2$, the non-inhibited print speed drops at the beginning and increases as exposure

time increases to 52 seconds, followed by a drop again. This case is not that conclusive with an irregular pattern, which could be partly because of experiment errors. However, it might also indicate that the inhibitors could contribute to the curing at longer exposure time as conjectured in Sections 3.1 and 3.2. Besides, the medium inhibition ratio $I_{UV}/I_{Blue} = 0.4$ generates a notable speed improvement for an exposure time of 36 second as well.

The observations jointly indicate that using a suitable combination of curing light intensity and inhibition light intensity, the PinCAM process can achieve a print speed that is comparable to traditional VPP-CAM processes for printing parts with desired geometrical fidelity. While

these results do not directly establish conclusive trends within the studied range and considering variations within experimental error, they offer indicative evidence suggesting a potential relationship between print speed and inhibition parameters. Further experiments are recommended to substantiate and refine the preliminary observations. Herein, our initial results together show that PinCAM holds the promise to improve the geometrical and surface properties without a significant sacrifice of print speed.

3.3.4. Microstructure

Since microstructure critically affects the quality and properties of fabricated parts, it is interesting to investigate the effect of inhibition on PinCAM microstructure [45-47]. It is worth noting that no post-processing (e.g., debinding, sintering) is required in this study, as the focus lies solely on evaluating the PinCAM processing itself. To achieve this, we conducted a preliminary characterization of the microstructures of our PinCAM-printed green ceramic samples using scanning electron microscopy (SEM). At this early stage, we aim to qualitatively evaluate the homogeneity, porosity, and any cluster agglomerations within the printed green ceramics. A recurring concern is the representativeness of the captured image for the sample. To address this, we meticulously scrutinized the sample preparation process to ensure unbiased particle deposition during the printing process. Additionally, we systematically examined and documented numerous particles at various magnifications, ultimately selecting representative images. This approach enhances the likelihood of an unbiased portrayal of the sample, albeit at the expense of significant time and resources. We also attempted SEM imaging of representative cured green ceramic samples at various resolutions and magnifications (see Appendix Figure A-7). Our SEM images reveal the microstructural features of the printed ceramics, including the formation of clusters for $I_{UV}/I_{Blue} = 0$ and the presence of porosity upon solidification due to polymerization (see Fig. 13). Small grain sizes appear in a concentrated density. The cluster agglomerations observed show a grain isotropy typical for VPP printing, as reported by other research studies [48-51].

Additionally, we characterize samples cured via different inhibition ratios for a high blue light intensity, to determine how they are affected by the inhibition ratio variations. By examining the apparent porosity as shown in the SEM images (Fig. 14), we can make a preliminary inference of the porosities and densities of the as-printed green ceramic samples. It appears that when there is no inhibition ($I_{UV}/I_{Blue}=0$), the printed sample exhibits small clusters and noticeably more pores compared to those cured by PinCAM with a non-zero inhibition ratio (I_{UV}/I_{Blue}). Increasing the inhibition ratio helps to smooth the texture, reduce the pores and particle agglomerations, and densify the ceramic part, making the sample more homogeneous, as confirmed by the elemental quantification analysis (see Appendix Figure A-8, Figure A-9 and Figure A-10).

Elemental mapping analysis using SEM and an energy-dispersive

detector (EDS) was employed to evaluate the distribution of aluminum (Al) and carbon (C) in the printed green bodies (Fig. 15). A noticeable disparity in the dispersion of Al and C was detected between samples printed with inhibition light and those without. The findings indicate that inhibition results in a more homogeneous distribution of Al within the polymer matrix compared to samples produced with the conventional VPP process, which exhibit noticeable clusters with varied compositions of C and Al. This improvement could reduce defects during subsequent debinding and sintering processes, when the green organic components are removed, thus enhancing the integrity of green bodies. The reason for this improvement may be that inhibition reduces the separation forces during the printing process, given that DLP-based VPP is a bottom-up process that requires a high separation force when each layer is removed from the resin chamber, causing delamination defects [50,52,53]. Further experiments are needed to validate this observation. Nevertheless, our experimental results consistently suggest that optimal curing light intensity and inhibition ratio are crucial for achieving Pin-CAM with high speed and high quality, including geometrical accuracy, surface finish, good density, and homogeneity.

3.4. Evaluating the PinCAM model

In this section, we aim to examine the validity of PinCAM models as presented in Section 2.3 for predicting print speed and cured part thickness. Specifically, experiment data and results (e.g., β , h_{UV} , h_{Blue} , E_c , D_n) from Sections 3.1 and 3.2 are used to estimate each sample's theoretical prediction of cured height by Eq. (9) and the corresponding process' maximum print speed by Eq. (10) (see Tables A-6 and A-7 for data). Further, the model predictions of sample height and maximum print speed are compared to the experiment result from Section 3.3, which provides the actual print speed and geometric dimensions with respect to the different curing light intensities and different I_{UV}/I_{Blue} ratios. As a systematical study of the PinCAM process, this comparison will allow us to evaluate the accuracy of using a simplified model that is initially developed for photo inhibited DLP to predict the PinCAM properties. It will also reveal the effects of curing and inhibition light intensities on the specific photo inhibited DLP-based ceramic printing process speed and part geometry. Moreover, it is expected that the experimentally validated analytical model will offer a tool to design the material system and two-wavelength exposure settings in the future for accomplishing an optimal PinCAM process.

Table A-8 presents a comparison between the curing height and print speed experimental values and the calculated predictions, which can be seen in Fig. 16. While the results aren't perfect, overall, both the experimental and predicted values converge to the same values, verifying the hypothesis that the use of inhibition can confine the horizontal profile curing and thus improve both lateral and horizontal dimensions.

The fact that most of the predicted values align closely with the ones

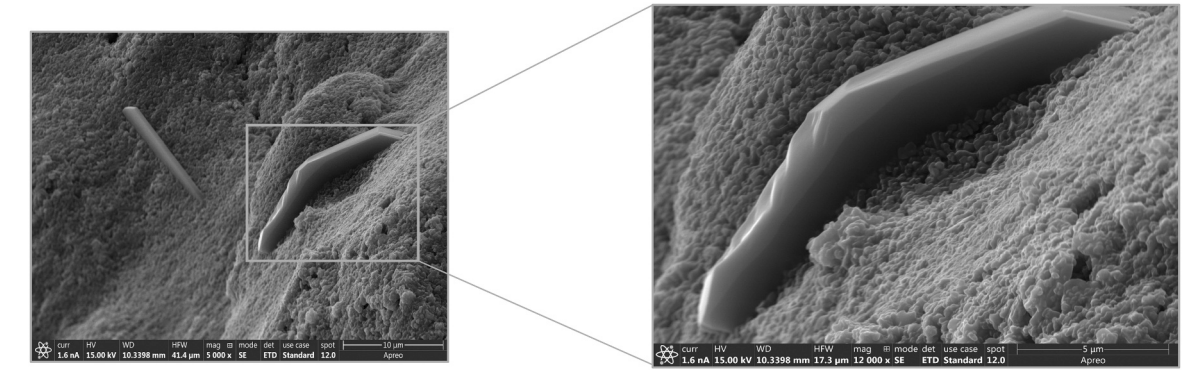


Fig. 13. SEM scan of ceramic samples printed using $I_{Blue} = 2.45 \text{ mW/cm}^2$ for a ratio of $I_{UV}/I_{Blue} = 0$. The images reveal the presence of cluster agglomerations within the cured green body of ceramics.

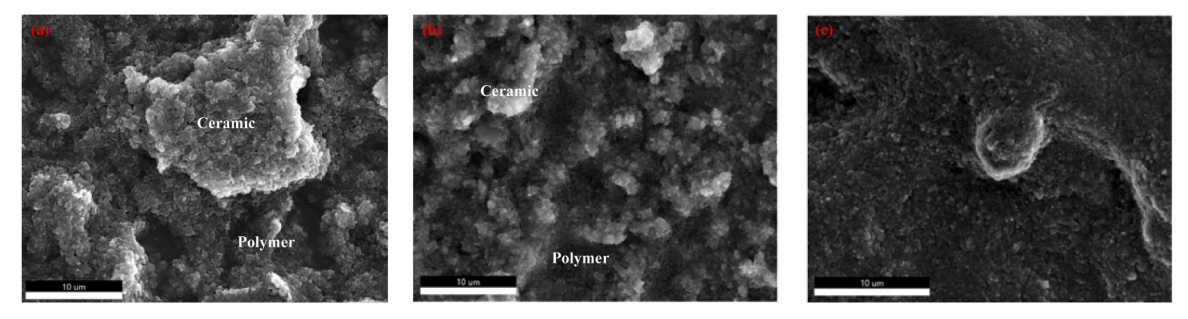


Fig. 14. SEM scans of the samples cured with varying inhibition ratios (a) $I_{UV}/I_{Blue} = 0$, (b) $I_{UV}/I_{Blue} = 0.8$, (d) $I_{UV}/I_{Blue} = 1.2$. As the inhibition ratio increases, the samples become more homogenous, with ceramic and polymer zones overlapping.

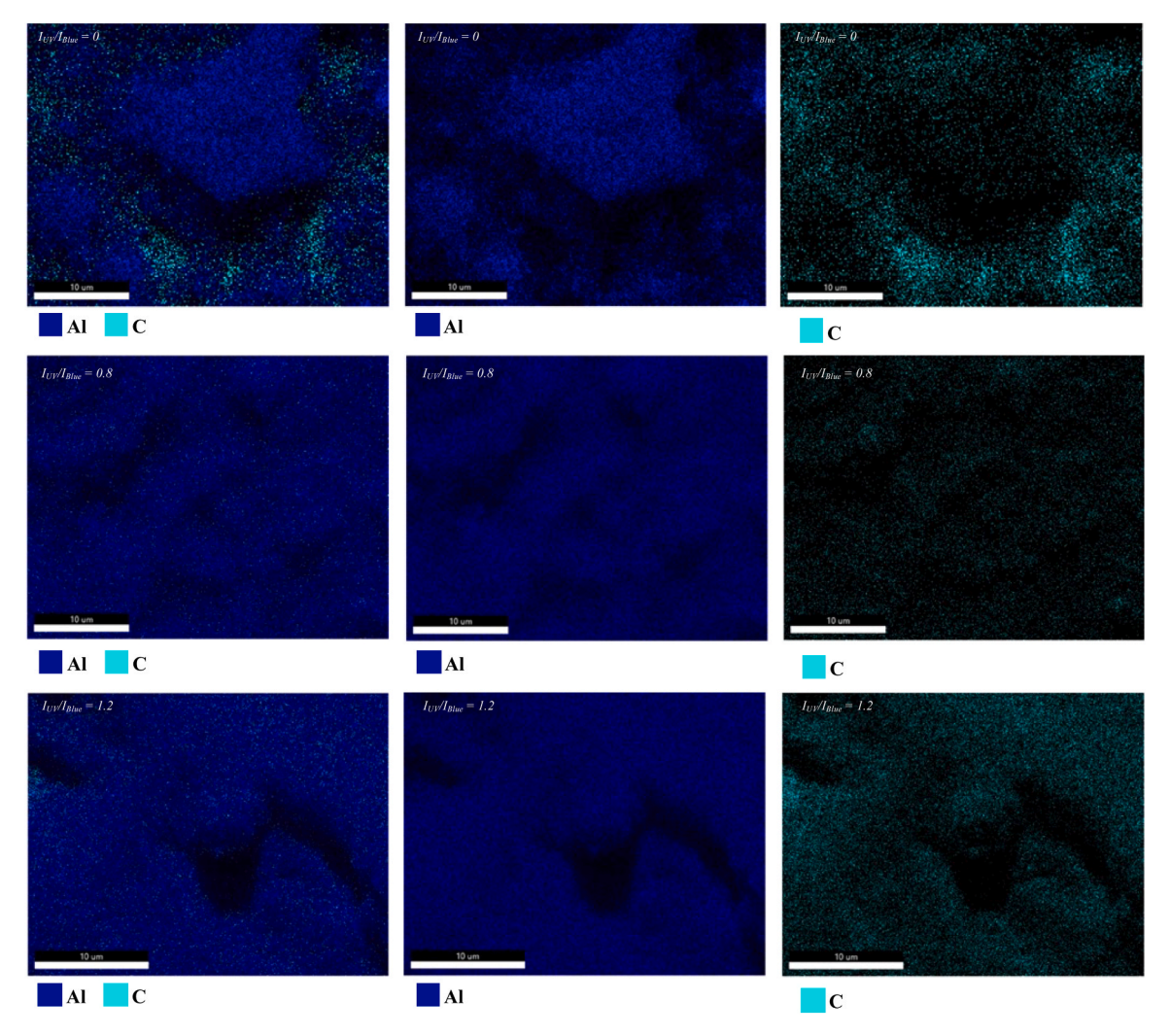


Fig. 15. SEM scans of the samples cured with varying inhibition ratios, showing the elemental composition of each sample (left: overlapping map of aluminum and carbon, center: alumina, right: carbon).

obtained through experimental testing suggests that the theory in Section 2.3 is applicable to PinCAM and the hypothesis proposed in this study is valid. While these findings are reliable and not mere chance occurrences, further research can allow for better comprehension of the trends and mechanisms examined to optimize the PinCAM process.

4. Conclusion

This first-of-its-kind, systematic study is aimed to pave the foundation of developing a new process - PinCAM as a potential approach to

improve the performance of VPP-based ceramic suspension printing and the resulting properties of as-printed green ceramic components. Our experiment results indicate that adding a second light to traditional VPP can offer an extra control variable for enhancing VPP-based ceramic printing. Specifically, PinCAM is shown to help enhance three-dimensional accuracy and resolution as well as reduce surface roughness, all with a decent exposure time or even less time especially compared to traditional approaches that would resort to lower curing light intensity. There is a promising basis for further studies to use the models and parameters discovered here to confirm the effectiveness of

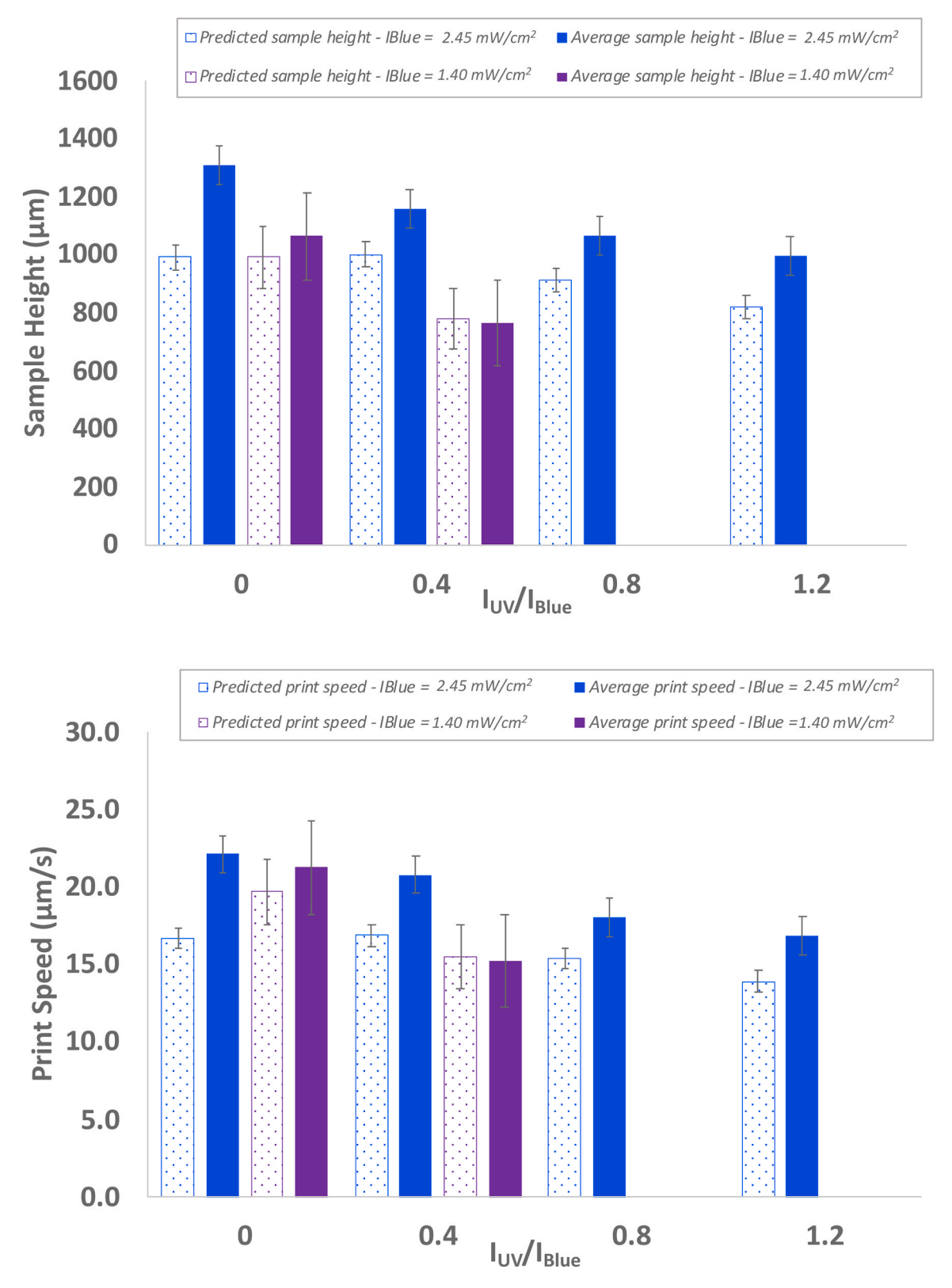


Fig. 16. Comparative analysis plot between experimental values and predicted values of sample height and print speed for varying inhibition ratios and two different blue light intensities $I_{Blue} = 2.45 \text{ mW/cm}^2$ and $I_{Blue} = 1.40 \text{ mW/cm}^2$. (Note: No data points under the inhibition ratios of 0.8 and 1.2 for $I_{Blue} = 1.40 \text{ mW/cm}^2$ due to no curing observed in these two cases.).

photo inhibition in printing geometrically precise models with higher print speeds. Ultimately, PinCAM will be developed to become a mature technology for allowing rapid fabrication of complex 3D ceramic components with accurate shapes and sizes as well as fine surface and

features.

The significant outcomes of this work can be summarized as follows:

- To the best of our knowledge, this is the first time that inhibition zone and working curve are characterized for the PinCAM process. A pilot study is conducted using two different levels of curing light intensity and several levels of inhibition ratio. The resulting inhibition parameters and E_c-D_pmodel can be used to pick a suitable process setting of PinCAM.
- We found that inhibition could reduce overcuring and increases the
 curing depth but only with a proper combination of inhibition and
 curing light intensities according to our observed inhibition and
 curing characteristics that exhibit different trends beyond certain
 level of inhibition ratio. This research study serves as a proof-ofconcept for future development of the PinCAM method at a larger
 scale.
- In general, increasing inhibition would slow down the print due to the consumption of the initiative species. However, the experiments conducted allow us to see that inhibition would significantly reduce print speed only for the lower region of exposure time (< 36 s in this case of using $I_{Bhue} = 2.45 \text{ mW/cm}^2$) and could be roughly the same fast as non-inhibited (conventional) VPP-CAM as the exposure time increases due to possible saturation of curing species at the higher region of exposure time. That is, the inhibited process speed could be close to the non-inhibited speed at certain exposure time with certain level of inhibition meanwhile. Our experiment results also indicate that employing medium inhibition levels provides enhanced control over three-dimensional over-curing, surface quality, green part porosity, and density with minimal impact on print speed. Compared to samples produced using conventional VPP processes, which exhibit heterogeneous agglomerations with varying composition percentages of ceramic and polymer particles, we observe that inhibition enables a more uniform distribution of ceramic and polymer particles within the green body.
- We also evaluated the applicability of general photo inhibition aided VPP process models for estimating the print height and speed of PinCAM. Both the experimental and predicted results converge, providing a theoretical basis for further modeling and optimizing the PinCAM processes.

Overall, this work proves that PinCAM has the potential to control the manufacturing of complex ceramic shapes precisely and efficiently through manipulating the complex interplay of photo inhibition and photo polymerization. Optimal inhibition and curing light intensities will facilitate a synergistic interplay to generate a favorable three-dimensional inhibition zone, which can prevent both vertical and horizontal over-curings and ease the part-substrate separation, thereby enhancing the print properties and process speed. Future research on the

PinCAM process should take into account the use of different preparation methods of the resin such as ball milling, as an alternative to magnetic stirring. This could open the door to studying how the resin suspension preparation procedures affect the characteristics of the printed samples. Other resin mixtures can also be tested for a chance to optimize the ceramics printing process. Moreover, printing in controlled atmospheres, such as a resin tank filled with an inert gas like nitrogen, can be introduced to study how the surface quality can be improved.

CRediT authorship contribution statement

Xiayun Zhao: Writing – review & editing, Writing – original draft, Supervision, Resources, Project administration, Methodology, Investigation, Funding acquisition, Formal analysis, Data curation, Conceptualization. Yousra Bensouda: Writing – review & editing, Writing – original draft, Visualization, Validation, Methodology, Investigation, Formal analysis, Data curation. Yue Zhang: Writing – review & editing, Validation, Methodology, Investigation, Formal analysis, Data curation.

Declaration of Competing Interest

The authors declare the following financial interests/personal relationships which may be considered as potential competing interests: Xiayun Zhao reports financial support was provided by the National Science Foundation under Faculty Early Career Development Award: CMMI-2238557, and the Manufacturing Pennsylvania Innovation Program Award #: 1060152–417945, through Carnegie Mellon University. Xiayun Zhao reports a relationship with University of Pittsburgh that includes: employment. Xiayun Zhao has patent #USPTO Application No.: 17/437,343 pending to USPTO. The reported photoinhibition-assisted photopolymerization-based ceramic additive manufacturing process is one embodiment and application of the filled pending patent above.

Acknowledgements

We acknowledge the fundings from 1) the National Science Foundation under Faculty Early Career Development Award: CMMI-2238557; and 2) the Manufacturing Pennsylvania Innovation Program (Award #: 1060152–417945, Source of Support: Carnegie Mellon University (Prime: Commonwealth of Pennsylvania)). Any opinions, findings, and conclusions or recommendations expressed in this publication are those of the authors and do not necessarily reflect the views of the National Science Foundation. Also, we would like to thank Dr. Jason Goldsmith and Kennametal Inc. who provided in-kind support and ceramic powders to conduct this work.

Appendix

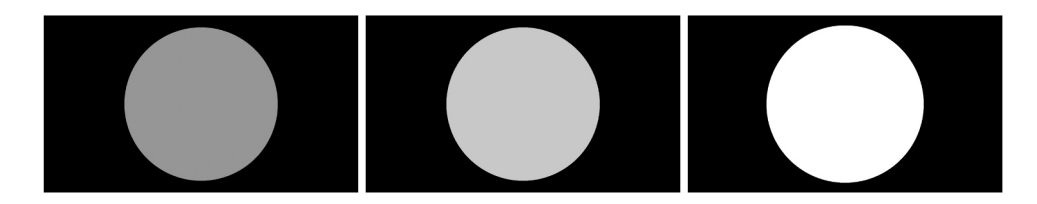


Figure A 1. Sample greyscale projection masks with varying light intensities generated by MATLAB code for blue light. Left to right: greyscale = 150, 200 and 255.

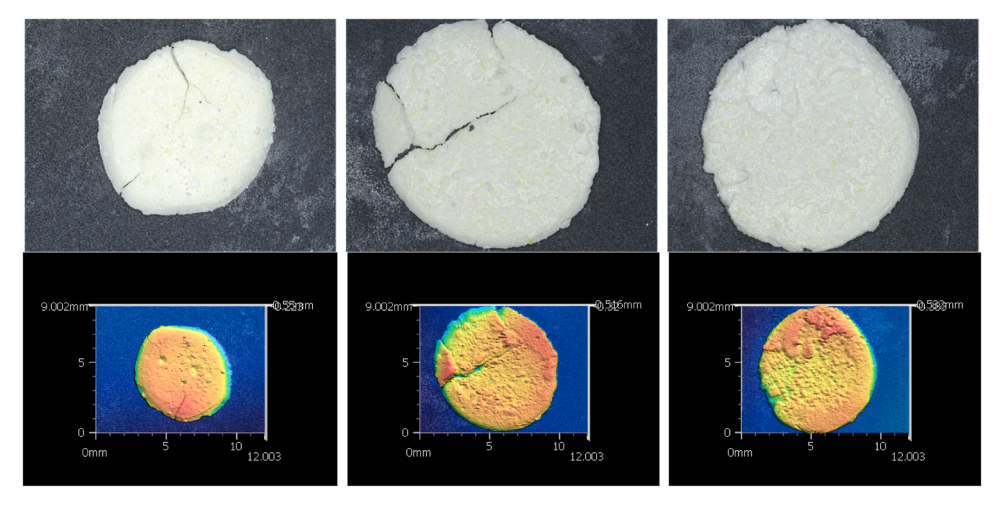


Figure A 2. Microscope image scans of some printed samples of green ceramic parts.

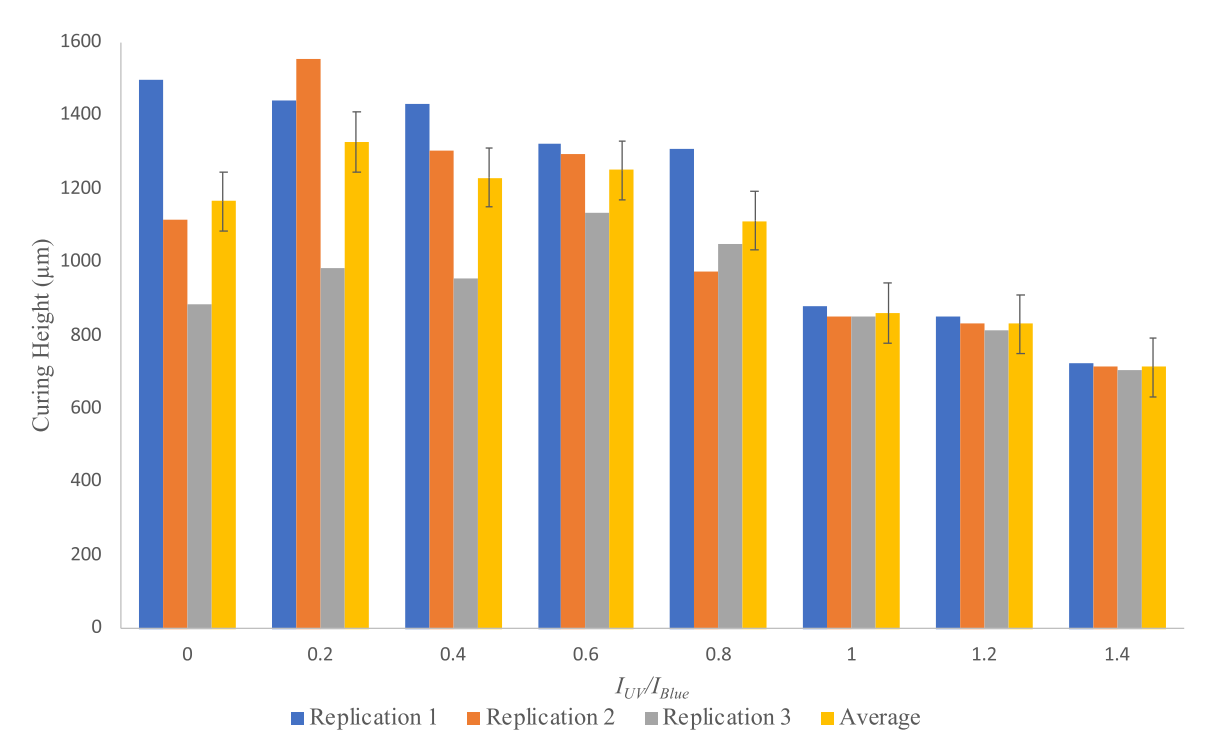


Figure A 3. Curing thickness variations for three experimental replications and their average using a high blue light intensity $I_{Blue} = 2.45 \text{ mW/cm}^2$.

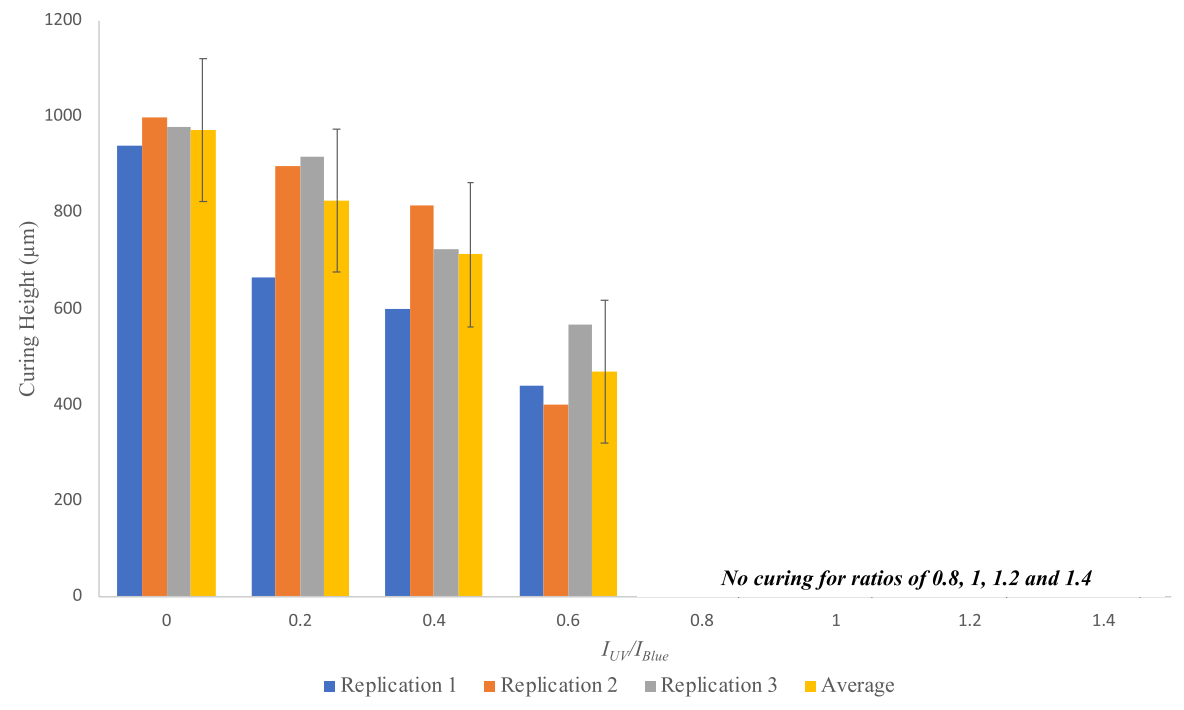


Figure A 4. Curing thickness variations for three experimental replications and their average using a low blue light intensity $I_{Blue} = 1.40 \text{ mW/cm}^2$.

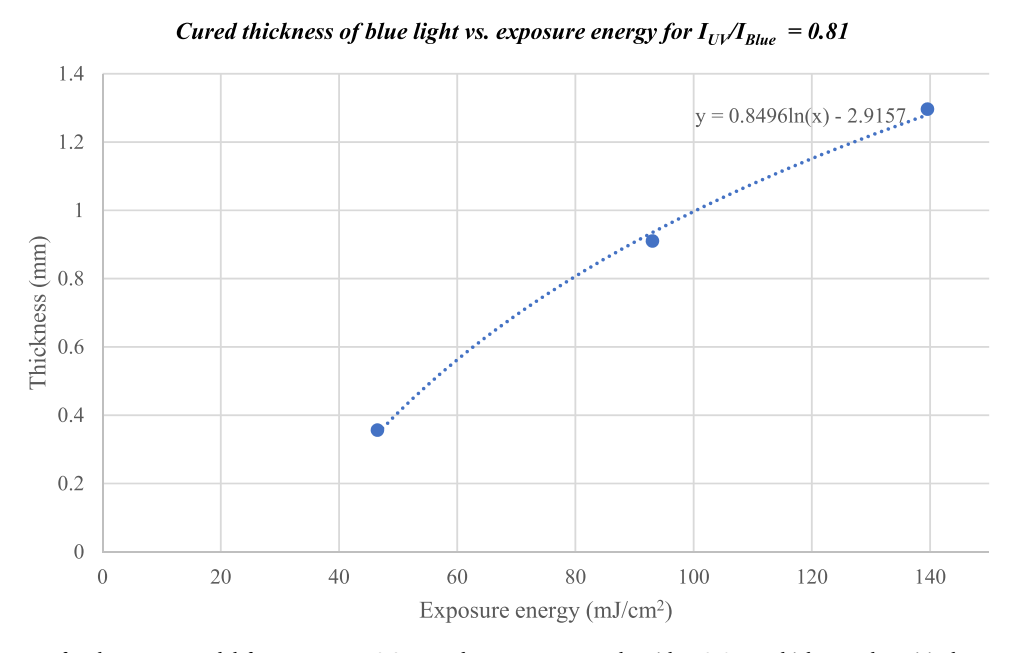


Figure A 5. Working curve for the E_c - D_p model for $I_{UV}/I_{Blue}=0.8$. In order to cure a sample with a 0.6 mm thickness, the critical exposure energy required is 62.68 mJ/cm^2 , which means that the exposure time should be around 26.94 s.

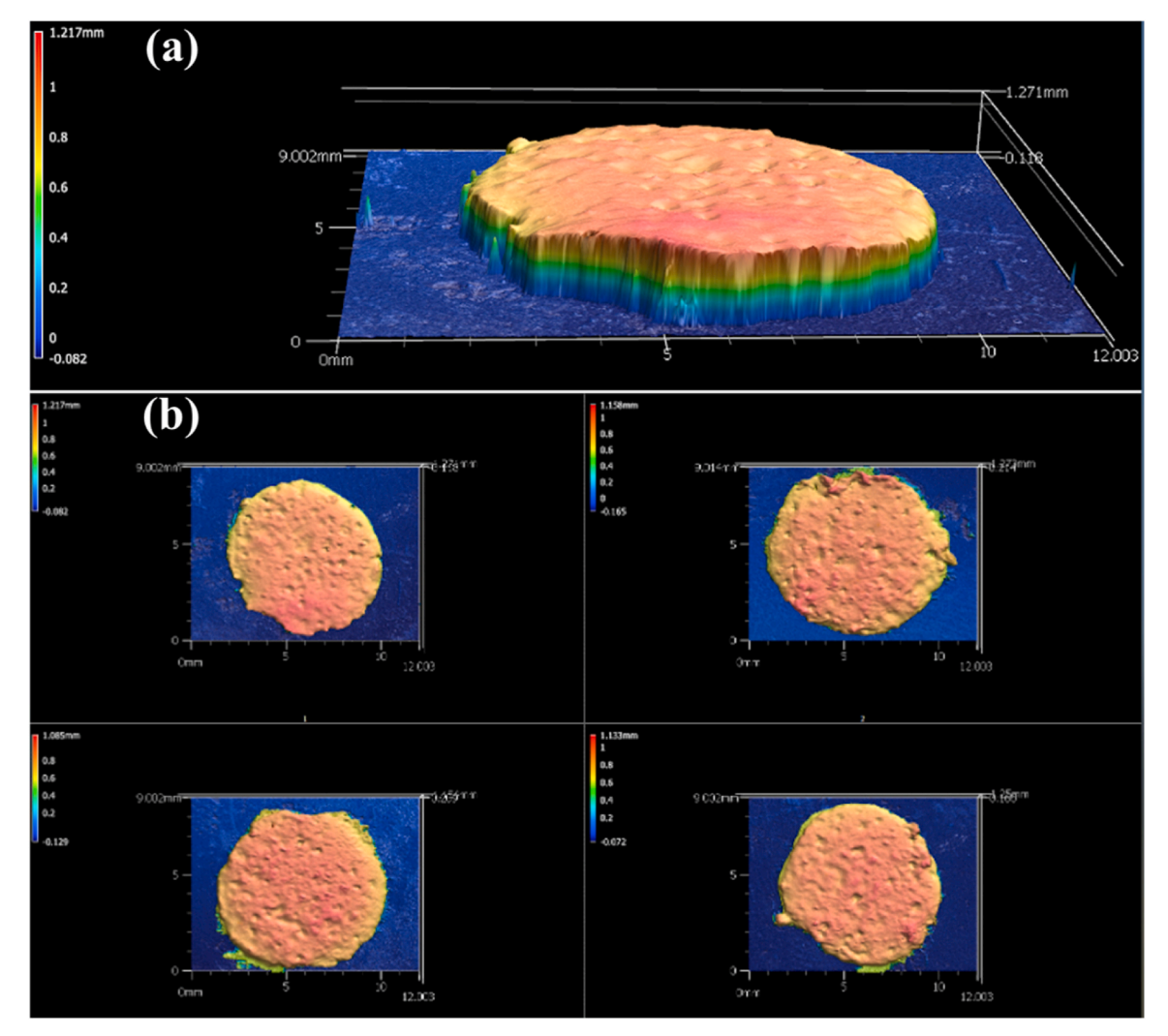


Figure A 6. 3D surface roughness topography of samples using the Keyence VR-3200. (a) isometric view, (b) top view.



 $\textbf{Figure A 7. SEM scans of the cured ceramic samples, observed at different resolutions and magnifications. (a) mag. $\times 250$, (b) mag. $\times 2500$, (c) mag. $\times 20,000$.}$

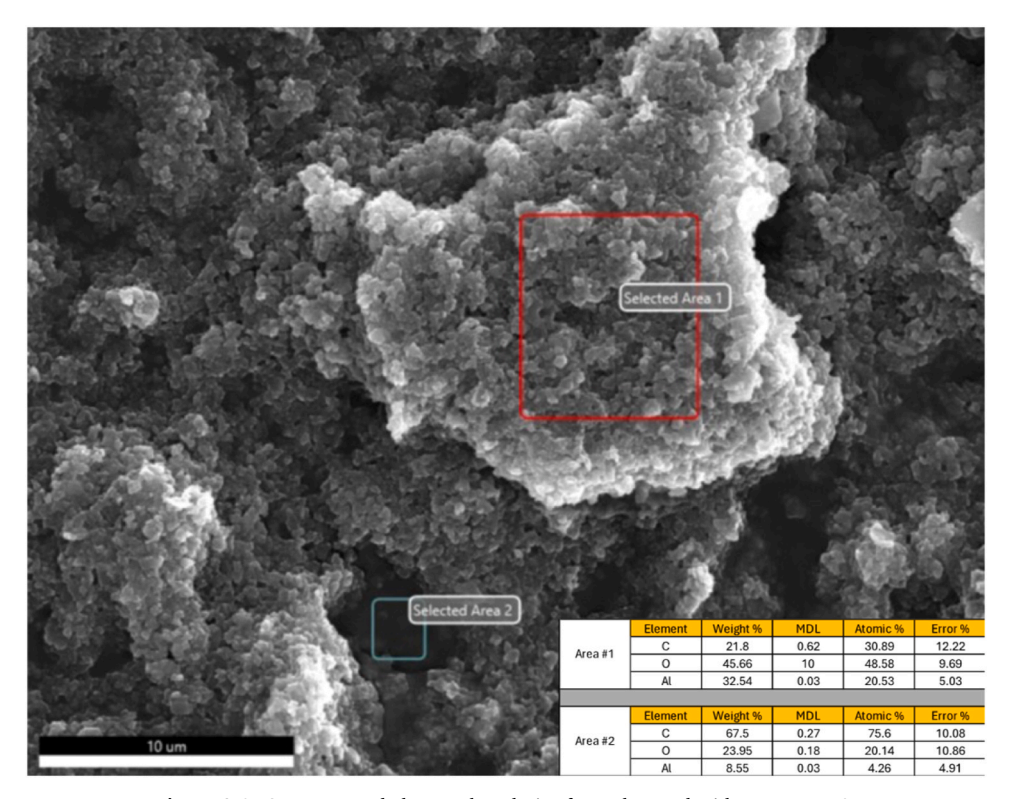


Figure A 8. SEM scan and elemental analysis of sample cured with $I_{UV}/I_{Blue}=0.$

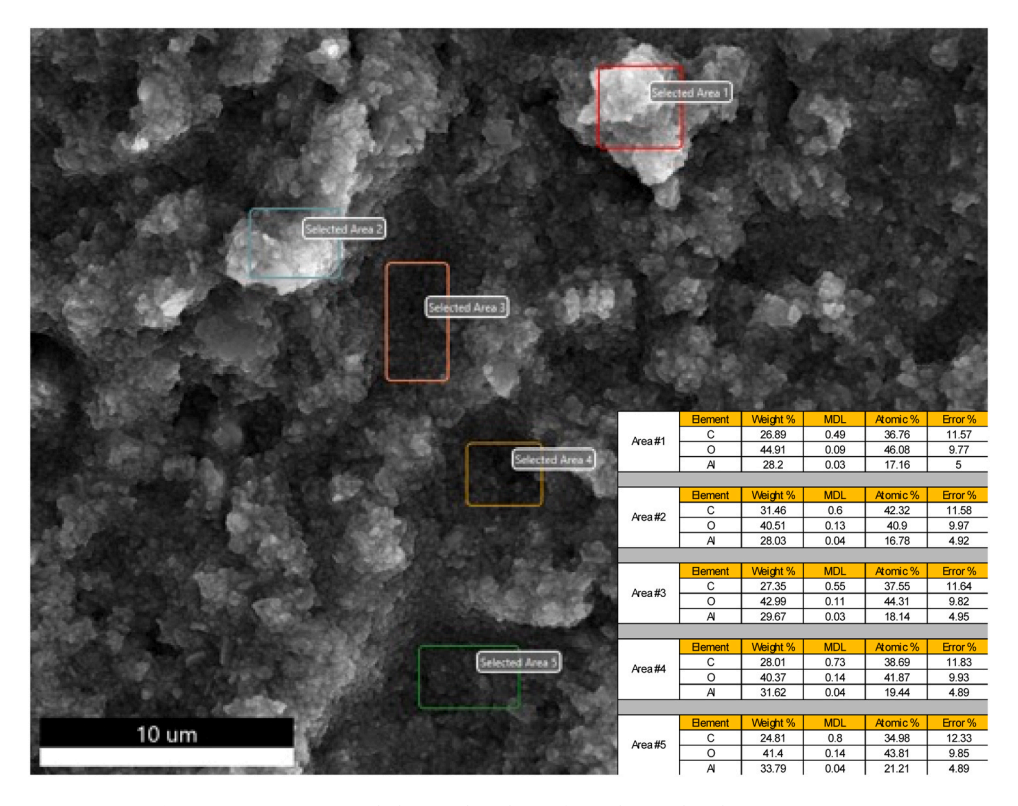


Figure A 9. SEM scan and elemental analysis of sample cured with $I_{UV}/I_{Blue}=0.8.$

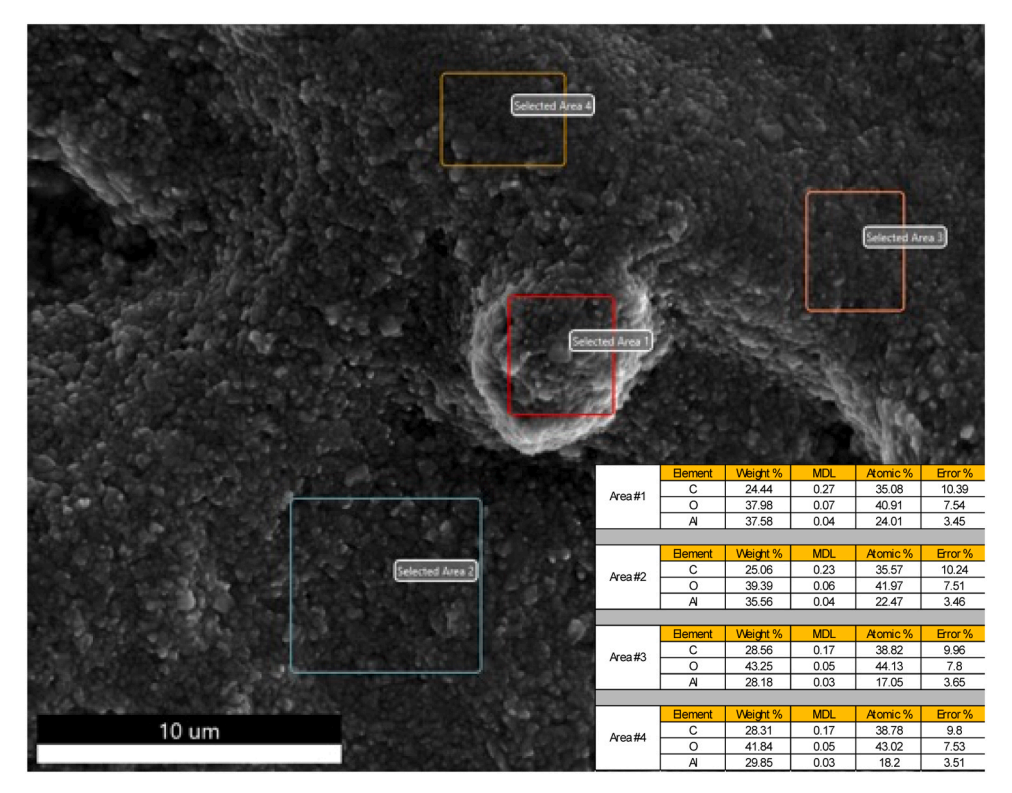


Figure A10. SEM scan and elemental analysis of sample cured with $I_{UV}/I_{Blue}=1.2$.

 $\label{eq:table A 1} \textbf{Inhibition zone height for different } I_{UV}/I_{Blue} \ ratios \ under \ two \ different \ levels \ of \ curing \ light \ intensity \ I_{Blue}.$

I _{Blue} intensity (mW/cm ²)	I_{UV}/I_{Blue} ratio	Exposure time (s)	Sample Height measured by Keyence Profilometer (µm)		Average Height (µm)	Standard Deviation	Inhib (µm)	ition zo	ne	Average Inhibition zone (µm)	Standard Deviation	
			R1	R2	R3			R1	R2	R3		
2.45	0	60	1499	1114	884	1165.67	310.74	0	0	0	0.00	0.00
	0.2		1441	1555	985	1327.00	301.62	58	-441	-101	-161.33	254.91
	0.4		1430	1305	953	1229.33	247.34	69	-191	-69	-63.67	130.08
	0.6		1320	1295	1136	1250.33	99.80	179	-181	-252	-84.67	231.09
	0.8		1309	975	1051	1111.67	175.07	190	139	-167	54.00	193.08
	1		879	853	849	860.33	16.29	620	261	35	305.33	295.01
	1.2		850	834	811	831.67	19.60	649	280	73	334.00	291.77
	1.4		723	713	705	713.67	9.02	776	401	179	452.00	301.75
1.4	0	60	940	1000	980	973.33	30.55	0	0	0	0.00	0.00
	0.2		664	898	917	826.33	140.91	276	102	63	147.00	113.41
	0.4		600	815	723	712.67	107.87	340	185	257	260.67	77.57
	0.6		439	401	566	468.67	86.41	501	599	414	504.67	92.55
	0.8											
	1		No cur	ing occur	s							
	1.2											
	1.4											

Table A 2Inhibition zone characterization parameters calculations.

I _{Blue} intensity (mW/cm ²)	I_{UV}/I_{Blue}	Inhibitio	Inhibition height (µm)		h _{Blue} (μm)			h _{UV} (μm)		Inhibition coefficient β	
		R1	R2	R3	R1	R2	R3	R1	R2	R3	
2.45	0	0.00	0.00	0.00	1720.00	600.00	1080.00	0.00	0.00	0.00	1
	0.4	110.00	10.00	340.00	3390.00	2670.00	890.00	-300.00	-30.00	-18,710.00	
	0.8	380.00	320.00	-20.00	780.00	1660.00	1940.00	970.00	3290.00	200.00	
	1.2	440.00	270.00	60.00	790.00	1360.00	1938.00	680.00	960.00	510.00	

(continued on next page)

Table A 2 (continued)

I _{Blue} intensity (mW/cm ²)	I_{UV}/I_{Blue}	Inhibiti	on height (μm)	h _{Blue} (μm)			<i>h_{UV}</i> (μm)			Inhibition coefficient β
		R1	R2	R3	R1	R2	R3	R1	R2	R3	
1.40	0	0.00	0.00	0.00	1180.00	2060.00	3220.00	0.00	0.00	0.00	
	0.4	60.00	370.00	320.00	2430.00	2090.00	1790.00	-160.00	-1670.00	-1460.00	

Table A-3 shows the E_c and D_p values for the three chosen I_{UV}/I_{Blue} ratios retrieved by curve fitting, for three different experimental replications – denoted as R1, R2, and R3 respectively.

Table A 3 $-E_c$ and D_p values under different I_{UV}/I_{Blue} ratios for two different curing light intensity I_{Blue} (Note: the red values are apparent outliers thus not included in the average calculation).

I _{Blue} curing light intensity (mW/cm ²)	I_{UV}/I_{Blue} ratio	E_c (mJ)				D_p (μ m))		
		R1	R2	R3	Average	R1	R2	R3	Average
2.45	0	6.07	0.03	2.82	4.44	387	133	251	319
	0.4	28.06	23.75	1.17	25.90	762	608	196	685
	0.8	29.45	15.38	14.24	19.69	567	379	434	460
	1.2	30.01	10.85	19.1	19.98	498	307	438	414
1.40	0	12.92	19.10	20.19	17.45	510	895	734	713
	0.4	15.452	14.22	10.85	13.51	553	475	395	474

Table A 4 –
Diameter measurements, vertical and volumetric printing speed calculations for two different levels of curing light intensity I_{Blue} with varying exposure time.

I _{Blue} intensity (mW/cm ²)	I_{UV}/I_{Blue} ratio	Exposure time (s)	Curing he	ight (μm)		Diameter	(µm)		Vertica	l printing	g speed (µm/s
			R1	R2	R3	R1	R2	R3	R1	R2	R3
2.45	0	20	744.00	967.00	826.00	5676.00	5654.00	5686.00	37.20	48.35	41.30
		28	1077.00	1091.00	711.00	5898.00	5986.00	5945.00	38.46	38.96	25.39
		36	1043.00	911.00	770.00	6230.00	6020.00	6288.00	28.97	25.31	21.39
		44	983.00	1345.00	893.00	6494.00	6650.00	6631.00	22.34	30.57	20.30
		52	1253.00	1021.00	1019.00	6719.00	6737.00	6782.00	24.10	19.63	19.60
		60	1227.00	1109.00	1039.00	6790.00	6851.00	6827.00	20.45	18.48	17.32
	0.4	20	404.00	585.00	734.00	4631.00	4811.00	4938.00	20.20	29.25	36.70
		28	624.00	383.00	670.00	4845.00	4173.00	5012.00	22.29	13.68	23.93
		36	972.00	754.00	913.00	5749.00	5739.00	5770.00	27.00	20.94	25.36
		44	1067.00	1165.00	979.00	5971.00	6098.00	6280.00	24.25	26.48	22.25
		52	1262.00	957.00	1124.00	6107.00	6680.00	6559.00	24.27	18.40	21.62
		60	1118.00	1096.00	702.00	6530.00	6599.00	6547.00	18.63	18.27	11.70
	0.8	20	369.00	539.00	459.00	4408.00	4712.00	5135.00	18.45	26.95	22.95
		28	325.00	450.00	725.00	5139.00	5596.00	5353.00	11.61	16.07	25.89
		36	581.00	476.00	842.00	5604.00	5630.00	5467.00	16.14	13.22	23.39
		44	904.00	947.00	1089.00	5966.00	6006.00	6026.00	20.55	21.52	24.75
		52	858.00	864.00	674.00	5886.00	6086.00	6153.00	16.50	16.62	12.96
		60	843.00	785.00	1061.00	6020.00	6119.00	6723.00	14.05	13.08	17.68
	1.2	20	319.00	440.00	413.00	4043.00	3717.00	4356.00	15.95	22.00	20.65
		28	361.00	589.00	523.00	4151.00	4222.00	4636.00	12.89	21.04	18.68
		36	404.00	739.00	798.00	4265.00	4426.00	4522.00	11.22	20.53	22.17
		44	722.00	568.00	715.00	5247.00	4500.00	5596.00	16.41	12.91	16.25
		52	769.00	752.00	708.00	6050.00	5867.00	6053.00	14.79	14.46	13.62
		60	786.00	841.00	983.00	6081.00	6450.00	6190.00	13.10	14.02	16.38
1.40	0	20	493.00	320.00	322.00	5218.00	5353.00	5094.00	24.65	16.00	16.10
		28	485.00	601.00	452.00	5417.00	5704.00	5538.00	17.32	21.46	16.14
		36	672.00	853.00	497.00	5628.00	5866.00	5316.00	18.67	23.69	13.81
		44	677.00	1174.00	841.00	5745.00	5992.00	5735.00	15.39	26.68	19.11
		52	903.00	1313.00	1034.00	5747.00	6031.00	5724.00	17.37	25.25	19.88
		60	1061.00	1144.00	1047.00	6041.00	6049.00	6306.00	17.68	19.07	17.45
	0.4	20	392.00	434.00	266.00	5074.00	4568.00	5311.00	19.60	21.70	13.30
		28	429.00	233.00	477.00	5101.00	5620.00	5594.00	15.32	8.32	17.04
		36	666.00	697.00	859.00	5615.00	5752.00	5720.00	18.50	19.36	23.86
		44	732.00	701.00	793.00	5657.00	5890.00	5558.00	16.64	15.93	18.02
		52	822.00	872.00	610.00	5709.00	5925.00	5476.00	15.81	16.77	11.73
		60	1004.00	779.00	729.00	5838.00	5600.00	5823.00	16.73	12.98	12.15

 $\label{eq:table A 5} \textbf{Surface roughness measurements for } I_{Blue} = 2.45 \text{ mW/cm}^2 \text{ and for } I_{Blue} = 1.40 \text{ mW/cm}^2 \text{ using the Keyence profilometer.}$

I_{Blue} curing light intensity (mW/cm ²)	I_{UV}/I_{Blue} ratio	Exposure time (s)	Surface rou	ighness S_a (μ m)		
			R1	R2	R3	Average
2.45	0	20	164	133	102	133.00
		28	136	138	94	122.67
		36	119	95	55	89.67
		44	105	200	107	137.33
		52	123	120	132	125.00
		60	134	152	113	133.00
	0.4	20	75	98	182	118.33
		28	97	64	112	91.00
		36	114	86	102	100.67
		44	207	142	126	158.33
		52	198	155	103	152.00
		60	174	116	101	130.33
	0.8	20	50	73	45	56.00
		28	46	79	91	72.00
		36	94	78	148	106.67
		44	172	19.5	159	116.83
		52	94	103	105	100.67
		60	74	86	122	94.00
	1.2	20	37	81	63	60.33
		28	54	64	105	74.33
		36	55	142	185	127.33
		44	108	113	160	127.00
		52	133	147	111	130.33
		60	121	125	142	129.33
1.40	0	20	39	53	38	43.33
		28	71	118	54	81.00
		36	75	122	64	87.00
		44	61	170	93	108.00
		52	92	253	167	170.67
		60	114	192	178	161.33
	0.4	20	63	82	37	60.67
		28	47	28	58	44.33
		36	77	143	95	105.00
		44	104	80	103	95.67
		52	120	145	106	123.67
		60	113	104	91	102.67

Table A 6 $H_{cure} \mbox{ and } S_{max} \mbox{ calculations for } I_{Blue} = 2.45 \mbox{ mW/cm}^2.$

I_{UV}/I_{Blue} ratio	h _{blue} (μm)	h_{UV} (μ m)	I_{UV} (mW/cm ²)	$E_c (\mathrm{mJ/cm}^2)$	S_{max} (μ m/s)	Hcure (µm)
0	1130	0	0	2.97	933.69	1376.55
						1541.67
						1665.00
						1763.48
						1845.47
						1915.69
0.4	2320	-6350	0.98	17.66	353.35	1031.71
						1370.72
						1623.94
						1826.13
						1994.45
						2138.63
0.8	2030	1490	1.96	19.69	148.81	806.84
						1103.48
						1325.05
						1501.96
						1649.24
						1775.40
1.2	1830	720	2.95	19.98	106.26	715.61
						983.03
						1182.76
						1342.25
						1475.02
						1588.75

$$\label{eq:Table A 7} \begin{split} \text{Hable A 7} \\ \text{H}_{cure} \text{ and } S_{max} \text{ calculations for } I_{Blue} = 1.40 \text{ mW/cm}^2. \end{split}$$

I_{UV}/I_{Blue} ratio	h _{blue} (μm)	h_{UV} (μ m)	I_{UV} (mW/cm ²)	$E_c (\mathrm{mJ/cm^2})$	S_{max} (μ m/s)	Hcure (µm)
0	3140	0	0	17.4	90.69	645.67
						1104.52
						1447.23
						1720.88
						1948.69
						2143.83
0.4	2320	-1100	0.55	13.51	110	732.30
						1071.32
						1324.53
						1526.72
						1695.04
						1839.22

 Table A 8

 Comparison between experimental and predicted print speed and height, under two blue light intensities for varying inhibition ratios.

I_{Blue} $I_{UV}/$ $(mW/$ I_{Blue}		Predicted Sample Height	Predicted Print Speed (µm/s)	Actual Sample Height (μm)		Actual Print Speed (μm/s)			Average Sample Height	Average Print Speed (µm/s)	Height Error (%)	Speed Error (%)	
cm ²)		(μm)		R1	R2	R3	R1	R2	R3	(µm)			
2.45	0	990	16.7	1440	1273	1202	24.4	21.6	20.4	1305.0	22.1	24.1	24.5
	0.4	1000	16.9	1160	1122	1184	19.7	19.0	23.7	1155.3	20.8	13.4	18.7
	0.8	910	15.4	1091	1086	1014	18.5	18.4	17.2	1063.7	18.0	14.4	14.6
	1.2	820	13.9	917	1082	991	15.5	18.3	16.8	996.7	16.9	17.7	17.5
1.40	0	990	19.7	996	977	1220	19.9	19.5	24.4	1064.3	21.3	7.0	7.3
	0.4	780	15.5	801	806	685	16.0	16.1	13.7	764.0	15.3	2.1	1.5

References

- J. Sun, et al., 3D printing of ceramic composite with biomimetic toughening design, Addit. Manuf. 58 (2022).
- [2] Revilla-Leon, M., et al., Flexural strength and Weibull characteristics of stereolithography additive manufactured versus milled zirconia. J Prosthet Dent, 2021. 125(4): p. 685-690.
- [3] G. Tan, et al., Nature-inspired nacre-like composites combining human tooth-matching elasticity and hardness with exceptional damage tolerance, Adv. Mater. 31 (52) (2019) e1904603.
- [4] S.A. Rasaki, et al., Photopolymerization-based additive manufacturing of ceramics: A systematic review, J. Adv. Ceram. 10 (3) (2021) 442–471.
- [5] S.M. C. Noè, A. Bouvet-Marchand, A. Graillot, C. Loubat, M. Sangermano, Cationic photopolymerization of bio-renewable epoxidized monomers, Prog. Org. Coat. 133 (2019) 131–138.
- [6] Y. Wang, et al., Printing depth modeling, printing process quantification and quick-decision of printing parameters in micro-vat polymerization, Mater. Des. (2023) 227.
- [7] M. Pagac, et al., A review of vat photopolymerization technology: materials, applications, challenges, and future trends of 3D printing, Polym. (Basel) 13 (4) (2021).
- [8] J.V. Crivello, E. Reichmanis, Photopolymer Materials and Processes for Advanced Technologies, Chem. Mater. 26 (1) (2013) 533–548.
- [9] P. Fiedor, et al., Photochemical study of a new bimolecular photoinitiating system for vat photopolymerization 3D printing techniques under visible light, Catalysts 10 (3) (2020).
- [10] J.R. Tumbleston, et al., Continuous liquid interface production of 3D objects, Science 347 (6228) (2015) 1349–1352.
- [11] S.M. Sajadi, et al., Damage-tolerant 3D-printed ceramics via conformal coating, Sci. Adv. 7 (28) (2021).
- [12] R. Janssen, S. Scheppokat, N. Claussen, Tailor-made ceramic-based components—Advantages by reactive processing and advanced shaping techniques, J. Eur. Ceram. Soc. 28 (7) (2008) 1369–1379.
- [13] O. Santoliquido, P. Colombo, A. Ortona, Additive manufacturing of ceramic components by digital light processing: a comparison between the "bottom-up" and the "top-down" approaches, J. Eur. Ceram. Soc. (2019).
- [14] Z. Chen, et al., 3D printing of ceramics: a review, J. Eur. Ceram. Soc. 39 (4) (2019) 661-687
- [15] W. Associates, 2022, 3D Printing and Additive Manufacturing Global State of the Industry..
- [16] S.P. Gentry, J.W. Halloran, Light scattering in absorbing ceramic suspensions: Effect on the width and depth of photopolymerized features, J. Eur. Ceram. Soc. 35 (6) (2015) 1895–1904.
- [17] A.Aa.M. Pumera, 3D-printing technologies for electrochemical applications, Chem. Soc. Rev. (10) (2016) 2740–2755.

- [18] D. Komissarenko, et al., DLP 3D printing of high strength semi-translucent zirconia ceramics with relatively low-loaded UV-curable formulations, Ceram. Int. 49 (12) (2023) 21008–21016.
- [19] S. Zakeri, M. Vippola, E. Levänen, A comprehensive review of the photopolymerization of ceramic resins used in stereolithography, Addit. Manuf. 35 (2020) 101177.
- [20] Y.-H. Lee, et al., Photocurable ceramic slurry using solid camphor as novel diluent for conventional digital light processing (DLP) process, J. Eur. Ceram. Soc. (2019).
- [21] C. Zhou, et al., Digital material fabrication using mask-image-projection-based stereolithography, Rapid Prototyp. J. 19 (3) (2013) 153–165.
- [22] A. Al Rashid, et al., Vat photopolymerization of polymers and polymer composites: Processes and applications, Addit. Manuf. 47 (2021).
- [23] H. Gong, et al., Optical Approach to Resin Formulation for 3D Printed Microfluidics, RSC Adv. 5 (129) (2015) 106621–106632.
- [24] D. Ahn, et al., Rapid High-Resolution Visible Light 3D Printing, ACS Cent. Sci. 6 (9) (2020) 1555–1563.
- [25] O. Santoliquido, P. Colombo, A. Ortona, Additive Manufacturing of ceramic components by Digital Light Processing: A comparison between the "bottom-up" and the "top-down" approaches, J. Eur. Ceram. Soc. 39 (6) (2019) 2140–2148.
- [26] Y. Ye, et al., 3D printing of integrated ceramic membranes by the DLP method, Ind. Eng. Chem. Res. 60 (26) (2021) 9368–9377.
- [27] Y. Liao, et al., 3D-printed complex microstructures with a self-sacrificial structure enabled by grayscale polymerization and ultrasonic treatment, ACS Omega 6 (28) (2021) 18281–18288.
- [28] L. Yue, et al., Single-vat single-cure grayscale digital light processing 3D printing of materials with large property difference and high stretchability, Nat. Commun. 14 (1) (2023) 1251.
- [29] L. Bourdon, et al., Improvements in resolution of additive manufacturing: advances in two-photon polymerization and direct-writing electrospinning techniques, ACS Biomater. Sci. Eng. 4 (12) (2018) 3927–3938.
- [30] S.D. Gittard, et al., Fabrication of microscale medical devices by two-photon polymerization with multiple foci via a spatial light modulator, Biomed. Opt. Express 2 (2011).
- [31] Z.C. Zhang, et al., Influence of the three-dimensional printing technique and printing layer thickness on model accuracy, J. Orofac. Orthop. 80 (4) (2019) 194–204.
- [32] M. Shahbazi, et al., Multimaterial 3D printing of self-assembling smart thermoresponsive polymers into 4D printed objects: a review, Addit. Manuf. 71 (2023).
- [33] R. Chaudhary, et al., Additive manufacturing by digital light processing: a review, Prog. Addit. Manuf. 8 (2) (2022) 331–351.
- [34] S. Song, et al., Effect of build orientation and layer thickness on manufacturing accuracy, printing time, and material consumption of 3D printed complete denture bases, J. Dent. 130 (2023) 104435.
- [35] A. Selimis, M.F, 3.8 laser-based 3D printing and surface texturing, Compr. Mater. Finish. 3 (2017) 111–136.

- [36] M. Vlasea, E. Toyserkani, Experimental characterization and numerical modeling of a micro-syringe deposition system for dispensing sacrificial photopolymers on particulate ceramic substrates, J. Mater. Process. Technol. 213 (11) (2013) 1970-1977
- [37] H.L. van der Laan, M.A. Burns, T.F. Scott, Volumetric photopolymerization confinement through dual-wavelength photoinitiation and photoinhibition, ACS Macro Lett. 8 (8) (2019) 899–904.
- [38] J. Wu, 2018, Constitutive modeling of photopolymerization and its application to 3D printing. 2018, Georgia Institute of Technology.
- [39] P. Prabhakaran, K.-S.L, Photopolymerization, Funct. Polym. (2019) 1–53.
- [40] I. Valizadeh, O.W, Parametric visco-hyperelastic constitutive modeling of functionally graded 3D printed polymers, Int. J. Mech. Sci. 226 (2022).
- [41] T. Hafkamp, et al., A feasibility study on process monitoring and control in vat photopolymerization of ceramics, Mechatronics 56 (2018) 220–241.
- [42] M.P. De Beer, et al., Rapid, continuous additive manufacturing by volumetric polymerization inhibition patterning, Sci. Adv. 5 (1) (2019) eaau8723.
- [43] P. Jacobs, Rapid Prototyping & Manufacturing: Fundamentals of StereoLithography, Society of Manufacturing Engineers, 1992.
- [44] B.W. Caplins, et al., Influence of spectral bandwidth on the working curve in vat photopolymerization, Addit. Manuf. 85 (2024).
- [45] E. Fiume, et al., Vat-photopolymerization of ceramic materials: exploring current applications in advanced multidisciplinary fields, Front. Mater. 10 (2023).

- [46] X. Wu, et al., Research progress of the defects and innovations of ceramic vat photopolymerization, Addit. Manuf. (2023).
- [47] A. Ottomaniello, et al., Highly conformable terahertz metasurface absorbers via two-photon polymerization on polymeric ultra-thin films, Nanophotonics 12 (8) (2023) 1557–1570.
- [48] X. Li, Y. Chen, Vat-Photopolymerization-Based Ceramic Manufacturing, Addit. Manuf. Process. (2020) 81–96.
- [49] Z. Xing, et al., Viscoelastic Paste-Based Ceramic vat Photopolymerization: Recent Achievements and Future Developments, Addit. Manuf. Front. 3 (1) (2024).
- [50] G. Nie, et al., Microstructure refinement-homogenization and flexural strength improvement of Al2O3 ceramics fabricated by DLP-stereolithography integrated with chemical precipitation coating process, J. Adv. Ceram. 10 (4) (2021) 200 208
- [51] S. Nohut, M. Schwentenwein, Vat photopolymerization additive manufacturing of functionally graded materials: a review, J. Manuf. Mater. Process. 6 (1) (2022).
- [52] K. Zhang, et al., A review of defects in vat photopolymerization additivemanufactured ceramics: characterization, control, and challenges, J. Eur. Ceram. Soc. 44 (3) (2024) 1361–1384.
- [53] K. Wang, et al., Study on defect-free debinding green body of ceramic formed by DLP technology, Ceram. Int. 46 (2) (2020) 2438–2446.